Journal of Computational Physics 529 (2025) 113890

Contents lists available at ScienceDirect

Journal of Computational Physics

journal homepage: www.elsevier.com/locate/jcp

Non-splitting Eulerian-Lagrangian WENO schemes for two-dimensional nonlinear convection-diffusion equations

Nanyi Zheng [a], Xiaofeng Cai [b,c,*], Jing-Mei Qiu [a], Jianxian Qiu [d]

[a] Department of Mathematical Sciences, University of Delaware, Newark, DE, 19716, USA
[b] Research Center for Mathematics, Advanced Institute of Natural Sciences, Beijing Normal University, Zhuhai 519087, China
[c] Guangdong Provincial Key Laboratory of Interdisciplinary Research and Application for Data Science, BNU-HKBU United International College, Zhuhai 519087, China
[d] School of Mathematical Sciences and Fujian Provincial Key Laboratory of Mathematical Modeling and High-Performance Scientific Computing, Xiamen University, Xiamen, Fujian 361005, China

ARTICLE INFO

Keywords:
Convection-diffusion
Eulerian-Lagrangian
Modified characteristic lines
WENO reconstruction
Mass conservation
Varying Lagrangian meshes

ABSTRACT

In this paper, we develop high-order, conservative, non-splitting Eulerian-Lagrangian (EL) Runge-Kutta (RK) finite volume (FV) weighted essentially non-oscillatory (WENO) schemes for convection-diffusion equations. The proposed EL-RK-FV-WENO scheme defines modified characteristic lines and evolves the solution along them, significantly relaxing the time-step constraint for the convection term. The main algorithm design challenge arises from the complexity of constructing accurate and robust reconstructions on dynamically varying Lagrangian meshes. This reconstruction process is needed for flux evaluations on time-dependent upstream quadrilaterals and time integrations along moving characteristics. To address this, we propose a strategy that utilizes a WENO reconstruction on a fixed Eulerian mesh for spatial reconstruction, and updates intermediate solutions on the Eulerian background mesh for implicit-explicit RK temporal integration. This strategy leverages efficient reconstruction and remapping algorithms to manage the complexities of polynomial reconstructions on time-dependent quadrilaterals, while ensuring local mass conservation. The proposed scheme ensures mass conservation due to the flux-form semi-discretization and the mass-conservative reconstruction on both background and upstream cells. Extensive numerical tests have been performed to verify the effectiveness of the proposed scheme.

1. Introduction

Simulating convection-diffusion phenomena has a wide range of applications, including fluid dynamics [43,28,13], materials science [37,40,9], and geophysics [36,35]. In this paper, we consider a scalar convection-diffusion equation:

$$u_t + \nabla_{\mathbf{x}} \cdot (\mathbf{F}(u, \mathbf{x}, t)) = \epsilon \Delta u, \tag{1.1}$$

where $\epsilon \geq 0$. Existing methods include the Eulerian [17,22] and Lagrangian approaches [15,5–7]. The Eulerian approach evolves the equation upon a fixed spatial mesh (or Eulerian mesh), and such methods are usually robust and relatively easy to implement, but

* Corresponding author at: Research Center for Mathematics, Advanced Institute of Natural Sciences, Beijing Normal University, Zhuhai 519087, China.
E-mail addresses: nyzheng@udel.edu (N. Zheng), xfcai@bnu.edu.cn (X. Cai), jingqiu@udel.edu (J.-M. Qiu), jxqiu@xmu.edu.cn (J. Qiu).

https://doi.org/10.1016/j.jcp.2025.113890
Received 19 June 2024; Received in revised form 11 January 2025; Accepted 22 February 2025

Available online 25 February 2025

they suffer from time-step constraints. The Lagrangian approach follows characteristics in time evolution by generating a Lagrangian mesh that moves with the velocity field, allowing for a larger time-step size compared with Eulerian schemes. However, the moving Lagrangian mesh can be greatly distorted, leading to significant challenges in analysis and implementation. Between the two approaches, there are the semi-Lagrangian (SL) approach [39,42,38,20], the Eulerian-Lagrangian (EL) approach [1,2,24,32,25,23,14] and the arbitrary Lagrangian-Eulerian (ALE) approach [10,31,45]. Both the SL and EL approaches utilize a fixed background mesh and accurately or approximately track information propagation along characteristics, which helps them ease the numerical time-step constraint, resulting in significant savings in CPU computation time [11]. The schemes from the ALE approach consider a dynamically moving mesh. These approaches aim to balance between the Eulerian and Lagrangian approaches in various ways, tailored for better efficiency of computational algorithms in different settings.

In this paper, we continue our development of the EL Runge-Kutta (RK) schemes [12,32], but now in a truly multi-dimensional finite volume (FV) fashion for nonlinear convection-diffusion problems. In the finite volume setting, we need to update only one degree of freedom per cell, as opposed to multiple ones, compared with the previous EL-RK discontinuous Galerkin (DG) scheme [12]. Building upon the EL-RK framework, we introduce a modified velocity field as a first-order approximation of the analytic velocity field, offering triple benefits: firstly, the modified velocity field has straight characteristic lines, leading to upstream cells with straight edges that are easier to be evaluated than polygons with curved edges; secondly, tracking characteristics approximately can allow a greatly relaxed time-stepping constraint compared with explicit Eulerian methods; thirdly, the EL framework offers flexibility in treating nonlinearity, while integrating diffusion terms, thereby presenting a truly multi-dimensional EL finite volume scheme compared to our earlier work in [20,32].

Although the introduction of the modified velocity field offers many benefits, it also presents new challenges in reconstructing high-order polynomials on dynamically varying Lagrangian upstream cells. Performing robust and accurate weighted essentially non-oscillatory (WENO) reconstructions on time-dependent upstream polygons can be computationally complex and expensive. Furthermore, performing high-order time integration along moving characteristics brings new complications in algorithm design. Below, we elaborate major computational roadblocks and our proposed strategy in the following two aspects:

- *Spatial reconstruction.* The EL RK formulation necessitates flux evaluations at the interface of upstream cells; thus, we need to reconstruct piecewise polynomials on upstream quadrilaterals. Performing WENO reconstruction of polynomials on distorted upstream quadrilaterals, e.g., see the red mesh in Fig. 2.2b, can be computationally involved. Further, shapes of these upstream cells differ in every time-step, leading to expensive mesh-dependent local computations. To address such challenges, we propose to (a) perform a robust and efficient WENO reconstruction of piecewise polynomials on the background Eulerian mesh; and (b) leverage a remapping algorithm to compute cell averages on upstream cells from cell averages on the background Eulerian mesh in a mass conservative fashion [27,44]. Finally, we perform piecewise polynomial reconstruction on upstream quadrilaterals, with preservation of cell averages computed in (b), while utilizing the piecewise polynomials on Eulerian mesh reconstructed in (a) for accuracy consideration.
- *Implicit-explicit (IMEX) RK temporal integration along linear approximation of characteristics.* A major computational challenge in performing method-of-lines time integrations along moving meshes is the complexity again in polynomial reconstructions of solutions on quadrilateral meshes that are time varying. To address this issue, we propose to update intermediate IMEX solutions at the background Eulerian mesh as in [20,32], for which efficient reconstruction and the remapping algorithms can be utilized to facilitate the polynomial reconstruction on time-dependent quadrilaterals as mentioned above.

We emphasize that efficient polynomial reconstruction on a fixed Eulerian mesh serves as a cornerstone in our EL-RK algorithm, upon which polynomial reconstructions on distorted upstream quadrilaterals are performed. Indeed, WENO reconstructions on a background Eulerian mesh have been well developed in the literature [30,21,46,18,44]. In this paper, we further improve upon our previous work [44] and propose a new 2D WENO reconstruction. This new approach strikes a good balance between controlling numerical oscillations and achieving optimal accuracy, by optimizing small stencil polynomial approximations and the weighting strategy.

The rest of the paper is organized as follows. Section 2 presents the proposed EL-RK-FV-WENO schemes; Section 3 presents extensive numerical results showcasing the scheme's effectiveness. Finally, we conclude in Section 4.

2. EL-RK-FV-WENO schemes

In Section 2.1, we introduce a first-order EL-RK-FV scheme for a linear convection-diffusion equation. Then, building upon the basic concepts introduced in Section 2.1, we discuss the construction of high-order EL-RK-FV-WENO schemes in Section 2.2. Finally, the extension of the proposed EL-RK-FV-WENO scheme to a nonlinear model is presented in Section 2.3.

2.1. First-order EL-RK-FV scheme

Consider

$$u_t + (a(x, y, t)u)_x + (b(x, y, t)u)_y = \epsilon(u_{xx} + u_{yy}). \tag{2.1}$$

We assume a rectangle computational domain denoted by $\Omega := [x_L, x_R] \times [y_B, y_T]$ with following partitions for each dimension

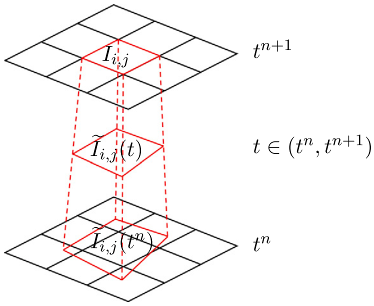

Fig. 2.1. Schematic illustration for the dynamic region $\widetilde{I}_{i,j}(t)$.

$$x_L = x_{\frac{1}{2}} < x_{\frac{3}{2}} < \ldots < x_{i-\frac{1}{2}} < x_{i+\frac{1}{2}} < \ldots < x_{N+\frac{1}{2}} = x_R,$$
$$y_B = y_{\frac{1}{2}} < y_{\frac{3}{2}} < \ldots < y_{j-\frac{1}{2}} < y_{j+\frac{1}{2}} < \ldots < y_{N+\frac{1}{2}} = y_T$$

with $x_i := (x_{i-\frac{1}{2}} + x_{i+\frac{1}{2}})/2$, $y_j := (y_{j-\frac{1}{2}} + y_{j+\frac{1}{2}})/2$, $\Delta x_i = x_{i+\frac{1}{2}} - x_{i-\frac{1}{2}}$, $\Delta y_j = y_{j+\frac{1}{2}} - y_{j-\frac{1}{2}}$, $I_i^x := [x_{i-\frac{1}{2}}, x_{i+\frac{1}{2}}]$, $I_j^y := [y_{j-\frac{1}{2}}, y_{j+\frac{1}{2}}]$ and $I_{i,j} := I_i^x \times I_j^y$, $\forall i, j$. We define the numerical solutions on the Eulerian mesh as $\{\overline{u}_{i,j}^n\}$, which approximate the averages of the $u(x, y, t^n)$ over the Eulerian cells $\{I_{i,j}\}$, i.e. $\{\frac{1}{|I_{i,j}|}\iint_{I_{i,j}} u(x, y, t^n)dxdy\}$.

To derive an EL-RK-FV formulation, we first define a modified velocity field $(\alpha(x, y, t), \beta(x, y, t))$. The definition of $(\alpha(x, y, t), \beta(x, y, t))$ is summarized as follows.

1. At $t = t^{n+1}$, $\alpha(x, y, t^{n+1})$ and $\beta(x, y, t^{n+1})$ belong to $Q^1(I_{i,j})$ satisfying
$$\begin{aligned} &\alpha(x_{i\pm\frac{1}{2}}, y_{j\pm\frac{1}{2}}, t^{n+1}) = a(x_{i\pm\frac{1}{2}}, y_{j\pm\frac{1}{2}}, t^{n+1}),\\ &\beta(x_{i\pm\frac{1}{2}}, y_{j\pm\frac{1}{2}}, t^{n+1}) = b(x_{i\pm\frac{1}{2}}, y_{j\pm\frac{1}{2}}, t^{n+1}). \end{aligned} \tag{2.2}$$
2. We define a dynamic region (see Fig. 2.1)
$$\widetilde{I}_{i,j}(t) := \{(x, y)|(x, y) = (\widetilde{x}(t; (\xi, \eta, t^{n+1})), \widetilde{y}(t; (\xi, \eta, t^{n+1}))), (\xi, \eta) \in I_{i,j}\}, \tag{2.3}$$
where $(\widetilde{x}(t; (\xi, \eta, t^{n+1})), \widetilde{y}(t; (\xi, \eta, t^{n+1})))$ represents the straight line going through (ξ, η, t^{n+1}) satisfying
$$\begin{cases} \widetilde{x}(t; (\xi, \eta, t^{n+1})) = \xi + (t - t^{n+1})\alpha(\xi, \eta, t^{n+1}),\\ \widetilde{y}(t; (\xi, \eta, t^{n+1})) = \eta + (t - t^{n+1})\beta(\xi, \eta, t^{n+1}). \end{cases} \tag{2.4}$$
We call (2.4) a modified characteristic line.
3. For $t \in [t^n, t^{n+1})$ and $(\widetilde{x}(t; (\xi, \eta, t^{n+1})), \widetilde{y}(t; (\xi, \eta, t^{n+1}))) \in \widetilde{I}_{i,j}(t)$,
$$\begin{cases} \alpha(\widetilde{x}(t; (\xi, \eta, t^{n+1})), \widetilde{y}(t; (\xi, \eta, t^{n+1}))) = \alpha(\xi, \eta, t^{n+1}),\\ \beta(\widetilde{x}(t; (\xi, \eta, t^{n+1})), \widetilde{y}(t; (\xi, \eta, t^{n+1}))) = \beta(\xi, \eta, t^{n+1}). \end{cases} \tag{2.5}$$

With the definitions above, we can derive

$$\begin{aligned} &\frac{d}{dt}\iint_{\widetilde{I}_{i,j}(t)} u(x, y, t)dxdy\\ &= \iint_{\widetilde{I}_{i,j}(t)} u_t(x, y, t)dxdy + \int_{\partial\widetilde{I}_{i,j}(t)} (\alpha, \beta)u \cdot \mathbf{n}ds\\ &= \iint_{\widetilde{I}_{i,j}(t)} u_t(x, y, t)dxdy + \iint_{\widetilde{I}_{i,j}(t)} \left[(au)_x + (bu)_y\right] dxdy\\ &\quad - \int_{\partial\widetilde{I}_{i,j}(t)} (a, b)u \cdot \mathbf{n}ds + \int_{\partial\widetilde{I}_{i,j}(t)} (\alpha, \beta)u \cdot \mathbf{n}ds\\ &= -\int_{\partial\widetilde{I}_{i,j}(t)} (a - \alpha, b - \beta)u \cdot \mathbf{n}ds + \epsilon\iint_{\widetilde{I}_{i,j}(t)} \Delta u dxdy. \end{aligned} \tag{2.6}$$

We define that $\mathbf{F}(u,x,y,t) := ((a-\alpha)u, (b-\beta)u)$ and provide the concise EL-FV formulation:

$$\frac{d}{dt}\iint\limits_{\widetilde{I}_{i,j}(t)} u(x,y,t)dxdy = -\int\limits_{\partial\widetilde{I}_{i,j}(t)} \mathbf{F}(u,x,y,t)\cdot\mathbf{n}ds + \epsilon\iint\limits_{\widetilde{I}_{i,j}(t)} \Delta u dxdy \\ := \mathcal{F}_{i,j}(u;t) + \mathcal{G}_{i,j}(u;t). \tag{2.7}$$

To evaluate the right-hand side (RHS) of (2.7), we introduce the following notation for semi-discretization:

$$\frac{d\widetilde{u}_{i,j}(t)}{dt} = \widetilde{\mathcal{F}}_{i,j}(\overline{\mathbf{U}};t) + \widetilde{\mathcal{G}}_{i,j}(\overline{\mathbf{U}};t), \quad i=1,\dots,N_x, \quad j=1,\dots,N_y, \tag{2.8}$$

where

- the notation $\widetilde{\cdot}$ specifies that the integral value corresponds to the characteristic spatial region $\widetilde{I}_{i,j}(t)$,
- $\widetilde{u}_{i,j}(t)$ approximates $\iint_{\widetilde{I}_{i,j}(t)} u(x,y,t)dxdy$,
- $\widetilde{\mathcal{F}}_{i,j}(\overline{\mathbf{U}};t)$ approximates $\mathcal{F}_{i,j}(u;t)$,
- $\widetilde{\mathcal{G}}_{i,j}(\overline{\mathbf{U}};t)$ approximates $\mathcal{G}_{i,j}(u;t)$,
- $\overline{\mathbf{U}} := \left(\overline{u}_{i,j}(t)\right)_{NxNy}$ represents the finite volumes such that

$$\overline{u}_{i,j}(t) \approx \frac{1}{|I_{i,j}|}\iint\limits_{I_{i,j}} u(x,y,t)dxdy. \tag{2.9}$$

Similar to $\overline{\mathbf{U}}$, we can also represent (2.8) globally as follows:

$$\frac{d\widetilde{\mathbf{U}}(t)}{dt} = \widetilde{\boldsymbol{\mathcal{F}}}(\overline{\mathbf{U}};t) + \widetilde{\boldsymbol{\mathcal{G}}}(\overline{\mathbf{U}};t), \tag{2.10}$$

where $\widetilde{\boldsymbol{\mathcal{F}}} := \left(\widetilde{\mathcal{F}}_{i,j}\right)_{N_xNy}$ and $\widetilde{\boldsymbol{\mathcal{G}}} := \left(\widetilde{\mathcal{G}}_{i,j}\right)_{N_xNy}$. Coupling (2.10) with the first-order forward-backward Euler IMEX method in [3] yields the first-order EL-RK-FV scheme:

$$\mathbf{M}\overline{\mathbf{U}}^{n+1} = \widetilde{\mathbf{U}}^n + \Delta t\widetilde{\boldsymbol{\mathcal{F}}}(\overline{\mathbf{U}}^n, t^n) + \Delta t\left(\epsilon\mathbf{MD}\overline{\mathbf{U}}^{n+1}\right), \tag{2.11}$$

where

- $\mathbf{M}$ is a diagonal matrix such that $\mathbf{M}\overline{\mathbf{U}}^{n+1} = \left(|I_{i,j}|\overline{u}_{i,j}^{n+1}\right)_{N_xN_y}$,
- $\widetilde{\mathbf{U}}^n$ approximates $\left(\iint_{\widetilde{I}_{i,j}(t^n)} u(x,y,t^n)dxdy\right)_{N_xN_y}$,
- $\mathbf{D}$ is a differential matrix such that

$$\mathbf{D}\overline{\mathbf{U}}^{n+1} \approx \left(\frac{1}{|I_{i,j}|}\iint\limits_{I_{i,j}} \Delta u dxdy\right)_{N_xN_y}.$$

As shown, the diffusion term in (2.11) is implicit. Consequently, $\overline{\mathbf{U}}^{n+1}$ is obtained by solving the following linear system:

$$\mathbf{M}(\mathbf{I} - \Delta t\epsilon\mathbf{D})\overline{\mathbf{U}}^{n+1} = \widetilde{\mathbf{U}}^n + \Delta t\widetilde{\boldsymbol{\mathcal{F}}}(\overline{\mathbf{U}}^n, t^n). \tag{2.12}$$

In (2.11), the methods for approximating the $\widetilde{\mathcal{F}}$ and $\widetilde{\mathcal{G}}$ terms with first-order accuracy are not discussed. High-order spatial approximations for these terms will be introduced in the next section. The first-order approximations can be viewed as simplified versions of their high-order counterparts.

Remark 2.1. (Empirical time-step constraint of the convection term for stability) Similar to the flux-form finite volume method in [34], where $\alpha = \beta = 0$, we require that

$$\Delta t \le \frac{1}{\frac{\max|a-\alpha|}{\Delta x} + \frac{\max|b-\beta|}{\Delta y}} = \frac{\Delta x\Delta y}{\Delta y\max|a-\alpha| + \Delta x\max|b-\beta|} \tag{2.13}$$

with $\Delta x := \max_{1\le i\le N_x}\{\Delta x_i\}$ and $\Delta y := \max_{1\le j\le N_y}\{\Delta y_j\}$. Furthermore, we stipulate that $\widetilde{I}_{i,j}(t^n)$ remains a convex quadrilateral. Otherwise, $\widetilde{I}_{i,j}(t^n)$ might become ill-posed in various situations. Therefore, it suffices to require that any three vertices of $\widetilde{I}_{i,j}(t^n)$ cannot be collinear. In other words,

$$\iint\limits_{\triangle_l(\widetilde{I}_{i,j}(t))} dxdy > 0, \quad l \in \{LT, RT, LB, RB\}, \tag{2.14}$$

where

$$\triangle_{LT}(\widetilde{I}_{i,j}(t)) := \{(x,y)|(x,y) = (\widetilde{x}(t;(\xi,\eta,t^{n+1})), \widetilde{y}(t;(\xi,\eta,t^{n+1}))), \tag{2.15}$$

$$y_{j-\frac{1}{2}} + (\xi - x_{i-\frac{1}{2}})\Delta y_j/\Delta x_i \le \eta \le y_{j+\frac{1}{2}},\ \xi \in [x_{i-\frac{1}{2}}, x_{i+\frac{1}{2}}]\}. \tag{2.16}$$

Similar definitions hold for the other $\{\triangle_l(\widetilde{I}_{i,j}(t))\}$. Through tedious derivation and omitting some higher-order terms, we can establish that (2.14) implies

$$\Delta t < \frac{1}{|a_x(x_i,y_j,t^{n+1})| + |b_y(x_i,y_j,t^{n+1})|}, \tag{2.17}$$

where $a_x(x_i,y_j,t^{n+1}) = \frac{\partial a}{\partial x}|_{(x_i,y_j,t^{n+1})}$ and $b_y(x_i,y_j,t^{n+1}) = \frac{\partial b}{\partial y}|_{(x_i,y_j,t^{n+1})}$. Here, we assume that the velocity field is smooth enough for us to take partial derivatives and drop the higher-order terms. By combining (2.13) with (2.17), and considering that $|a-\alpha|, |b-\beta| = O(\Delta t) + O(\Delta x^2) + O(\Delta y^2)$, we arrive at an approximate time-step constraint:

$$\Delta t \sim \sqrt{\min\{\Delta x, \Delta y\}}. \tag{2.18}$$

2.2. High-order EL-RK-FV-WENO schemes

In this section, we introduce the high-order EL-RK-FV-WENO schemes by first focusing on constructing the high-order approximations of the convection and the diffusion terms of the semi-discretization (2.8) in Section 2.2.1 and Section 2.2.2 respectively. Finally, the coupling of the semi-discretization with high-order IMEX RK methods is discussed in Section 2.2.3.

2.2.1. Flux approximation

As analyzed in Remark 2.1, the design of the flux function at the boundaries of dynamically changing, nonuniform Lagrangian cells significantly relaxes the time-step constraint. However, compared to the flux function of the Eulerian approach, located at $\{\partial I_{i,j}\}$, this brings significant challenges in terms of designing an efficient spatial discretization for such a framework. To address this, our strategy contains three basic steps. First, we conduct an efficient WENO-type reconstruction on the fixed Eulerian mesh. Second, an efficient remapping procedure is designed to map the piecewise WENO reconstruction polynomial with respect to the Eulerian mesh $\{I_{i,j}\}$ to another piecewise polynomial with respect to the Lagrangian mesh $\{\widetilde{I}_{i,j}(t)\}$. Finally, we use the new piecewise polynomial to provide upwind point values at the boundaries of $\{\partial\widetilde{I}_{i,j}(t)\}$ and approximate the flux function. The details of these three steps are concluded as follows:

Step 1: *Construct a piecewise polynomial with respect to the Eulerian mesh,* $\{I_{i,j}\}$.
We construct a piecewise reconstruction polynomial $u^{\text{WENO}}(x,y)$ such that
- $u^{\text{WENO}}(x,y)|_{I_{i,j}} = u^{\text{WENO}}_{i,j}(x,y)$ with $u^{\text{WENO}}_{i,j} \in P^2(I_{i,j})$ for all i,j,
- each $u^{\text{WENO}}_{i,j}$ is constructed based on the information $\overline{u}_{i,j}(t)$ along with its eight neighbor finite volumes,
- $\iint_{I_{i,j}} u^{\text{WENO}}(x,y)dxdy = \Delta x_i \Delta y_j \overline{u}_{i,j}(t)$ for all i,j,
- $u^{\text{WENO}}(x,y) = u(x,y,t) + O(\Delta x^3) + O(\Delta y^3)$, $(x,y) \in \Omega$.

Here, we summarize the details of constructing $u^{\text{WENO}}(x,y)$ in Appendix A for conciseness. A schematic is offered in Fig. 2.2a to demonstrate the discontinuity of $u^{\text{WENO}}(x,y)$. We use various colors to shade different Eulerian cells, indicating that $u^{\text{WENO}}(x,y)$ has distinct polynomial expressions in each cell. In the schematic, the tildes over i and j are used on purpose, which will be used in the following steps. We would like to emphasize that the WENO-ZQ reconstruction method introduced in Appendix A is a more advanced version than the one we previously designed, as detailed in [44]. In particular, in the numerical section, we observe that the solution of the WENO reconstruction in [44] introduces a small numerical wiggle. We redesigned the small stencils and part of the weighting strategy. The newly designed WENO-ZQ method presented in this paper significantly enhances the control of numerical oscillation, addressing the suboptimal performance of the previously designed method in managing nonphysical oscillations.

Step 2: *Construct a piecewise polynomial on the Lagrangian mesh* $\{\widetilde{I}_{i,j}(t)\}$ *(Remapping).*
Step 1 is an efficient reconstruction method and is inevitable, as will be shown in Section 2.2.3. The basic idea of this remapping step is that we want to conduct an efficient modification to $u^{\text{WENO}}(x,y)$ instead of involving a new reconstruction on the Lagrangian mesh. The resulting new piecewise polynomial, denoted by $\widetilde{u}^{\text{WENO}}(x,y)$, satisfies the following conditions:
- $\widetilde{u}^{\text{WENO}}(x,y)|_{\widetilde{I}_{i,j}(t)} = \widetilde{u}^{\text{WENO}}_{i,j}(x,y)$ with $\widetilde{u}^{\text{WENO}}_{i,j} \in P^2(\widetilde{I}_{i,j}(t))$ for all i,j,
- $\iint_{\widetilde{I}_{i,j}(t)} \widetilde{u}^{\text{WENO}}(x,y)dxdy = \iint_{\widetilde{I}_{i,j}(t)} u^{\text{WENO}}(x,y)dxdy$ for all i,j,
- $\widetilde{u}^{\text{WENO}}(x,y) = u(x,y,t) + O(\Delta x^3) + O(\Delta y^3)$, $(x,y) \in \Omega$.

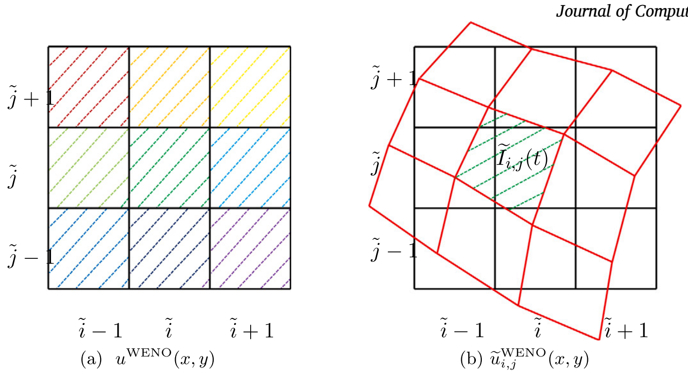

Fig. 2.2. Schematic illustrations of $u^{\mathrm{WENO}}(x, y)$ and $\widetilde{u}^{\mathrm{WENO}}_{i,j}(x, y)$. (For interpretation of the colors in the figure(s), the reader is referred to the web version of this article.)

Here, the first condition refers to the capacity of $\widetilde{u}^{\mathrm{WENO}}(x, y)$ to provide upwind point value information for the flux approximation, the second condition is related to the mass conservation property, and the third one is an accuracy requirement. We summarize the procedure for constructing $\widetilde{u}^{\mathrm{WENO}}(x, y)$ in a given Lagrangian cell, $\widetilde{I}_{i,j}(t)$, as follows (see Fig. 2.2b):

Step 2.1: Compute the exact "mass" of $u^{\mathrm{WENO}}(x, y)$ over $\widetilde{I}_{i,j}(t)$, i.e.

$$\widetilde{u}_{i,j} := \iint\limits_{\widetilde{I}_{i,j}(t)} u^{\mathrm{WENO}}(x, y)\,dx\,dy. \tag{2.19}$$

The integrand in Equation (2.19) is discontinuous over $\widetilde{I}_{i,j}(t)$. A numerical integral for Equation (2.19) contains two basic steps. First, a clipping procedure is conducted to divide $\widetilde{I}_{i,j}(t)$ into smaller polygons such that $u^{\mathrm{WENO}}(x, y)$ is continuous in each of them. Second, a numerical integration is conducted in each polygon, and the results are summed to obtain the final integral. Following these two basic steps, there are different implementation methods [16,27,44]. For a detailed implementation, we refer to our previous work [44].

Step 2.2: Find all Eulerian cells that intersect with $\widetilde{I}_{i,j}(t)$. We define that $\mathcal{K} := \{(p, q) | I_{p,q} \cap \widetilde{I}_{i,j}(t) \neq \emptyset\}$. For instance, in Fig. 2.2b, $\mathcal{K} = \{(\tilde{i}-1, \tilde{j}+1), (\tilde{i}, \tilde{j}+1), (\tilde{i}-1, \tilde{j}), (\tilde{i}, \tilde{j}), (\tilde{i}, \tilde{j}-1)\}$. Here, the tildes over i and j are used to distinguish the cell indices in $\mathcal{K}$ from (i, j), as the upstream cell $\widetilde{I}_{i,j}(t)$ may be distant from the Eulerian cell $I_{i,j}$ when large time step sizes are used.

Step 2.3: Compute the integrals of the candidate P^2 polynomials over $\widetilde{I}_{i,j}(t)$, i.e.

$$\widetilde{u}^{p,q}_{i,j} := \iint\limits_{\widetilde{I}_{i,j}(t)} u^{\mathrm{WENO}}_{p,q}(x, y)\,dx\,dy, \quad (p, q) \in \mathcal{K}. \tag{2.20}$$

Step 2.4: Choose the index $(\tilde{p}, \tilde{q})$ such that $|\widetilde{u}^{p,q}_{i,j} - \widetilde{u}_{i,j}|$ reaches the minimum, i.e.

$$|\widetilde{u}^{\tilde{p},\tilde{q}}_{i,j} - \widetilde{u}_{i,j}| = \min_{(p,q)\in\mathcal{K}} \{|\widetilde{u}^{p,q}_{i,j} - \widetilde{u}_{i,j}|\}. \tag{2.21}$$

Step 2.5: Define a P^2 polynomial, denoted by $\widetilde{u}^{\mathrm{WENO}}_{i,j}(x, y)$, on $\widetilde{I}_{i,j}(t)$ such that

$$\widetilde{u}^{\mathrm{WENO}}_{i,j}(x, y) := u^{\mathrm{WENO}}_{(\tilde{p},\tilde{q})}(x, y)|_{\widetilde{I}_{i,j}(t)} - \frac{1}{|\widetilde{I}_{i,j}(t)|}\widetilde{u}^{(\tilde{p},\tilde{q})}_{i,j} + \frac{1}{|\widetilde{I}_{i,j}(t)|}\widetilde{u}_{i,j}, \tag{2.22}$$

where $\cdot|_{\widetilde{I}_{i,j}(t)}$ means that we redefine the domain of definition to be $\widetilde{I}_{i,j}(t)$ for a given function. As an example, consider the case demonstrated in Fig. 2.2b where $(\tilde{p}, \tilde{q}) = (\tilde{i}, \tilde{j})$. In this case, we simply change the domain of definition for $u^{\mathrm{WENO}}_{\tilde{i},\tilde{j}}(x, y)$ and adjust it according to (2.22).

Step 3: *Construct the final flux approximation.*
The final flux approximation is given by the following conservative formulation

$$\widetilde{\mathcal{F}}_{i,j}(\overline{\mathbf{U}}; t) := -\int\limits_{\partial\widetilde{I}_{i,j}(t)} \hat{F}\left(\widetilde{u}^{\mathrm{WENO}}, x, y, t\right) ds, \tag{2.23}$$

where

$$\hat{F}\left(\widetilde{u}^{\mathrm{WENO}}, x, y, t\right) := W(x, y, t)\widetilde{u}^{\mathrm{up}}_{i,j}(x, y) \tag{2.24}$$

with

$$W(x,y,t) := (a-\alpha, b-\beta)\cdot \mathbf{n} \tag{2.25}$$

and

$$\widetilde{u}^{\text{up}}_{i,j}(x,y) := \begin{cases} \widetilde{u}^{\text{WENO}}_{i,j}(x,y), & W>0,\\ \widetilde{u}^{\text{WENO,ext}}_{i,j}(x,y), & W\le 0. \end{cases} \tag{2.26}$$

Here, $\widetilde{u}^{\text{WENO,ext}}_{i,j}(x,y)$ are the exterior solution with respect to corresponding edge of $\widetilde{I}_{i,j}(t)$.

At the end of this section, we prove two basic properties of $\widetilde{u}^{\text{WENO}}(x,y)$.

Proposition 2.2. *(Mass conservation for the remapping method) Local integrals of $\widetilde{u}^{WENO}$ over $\{\widetilde{I}_{i,j}(t)\}$ are consistent with the integrals of u^{WENO}.*

Proof.

$$\begin{aligned} &\iint\limits_{\widetilde{I}_{i,j}(t)} \widetilde{u}^{\text{WENO}}(x,y)\,dx\,dy\\ =&\iint\limits_{\widetilde{I}_{i,j}(t)} \left(u^{\text{WENO}}_{(\tilde p,\tilde q)}(x,y)|_{\widetilde{I}_{i,j}(t)} - \frac{1}{|\widetilde{I}_{i,j}(t)|}\widetilde{u}^{(\tilde p,\tilde q)}_{i,j} + \frac{1}{|\widetilde{I}_{i,j}(t)|}\widetilde{u}_{i,j}\right) dx\,dy\\ =&\ \widetilde{u}^{(\tilde p,\tilde q)}_{i,j} - \widetilde{u}^{(\tilde p,\tilde q)}_{i,j} + \widetilde{u}_{i,j}\\ =&\iint\limits_{\widetilde{I}_{i,j}(t)} u^{\text{WENO}}(x,y)\,dx\,dy. \quad\square \end{aligned} \tag{2.27}$$

Proposition 2.3. *(Accuracy of the remapping method) Assuming $u(x,y,t)$ is sufficiently smooth and $\Delta x\sim\Delta y$, we have the following estimate for $\widetilde{u}^{WENO}$:*

$$\widetilde{u}^{WENO}(x,y) = u(x,y,t) + O(\Delta x^3). \tag{2.28}$$

Proof. For $(\widetilde{x},\widetilde{y})\in \widetilde{I}_{i,j}(t)$,

$$\begin{aligned} &\widetilde{u}^{\text{WENO}}(\widetilde{x},\widetilde{y}) - u(\widetilde{x},\widetilde{y},t)\\ =&\left(u^{\text{WENO}}_{(\tilde p,\tilde q)}(\widetilde{x},\widetilde{y})|_{\widetilde{I}_{i,j}(t)} - \frac{1}{|\widetilde{I}_{i,j}(t)|}\widetilde{u}^{(\tilde p,\tilde q)}_{i,j} + \frac{1}{|\widetilde{I}_{i,j}(t)|}\widetilde{u}_{i,j}\right) - u(\widetilde{x},\widetilde{y},t)\\ =&\left(u^{\text{WENO}}_{(\tilde p,\tilde q)}(\widetilde{x},\widetilde{y})|_{\widetilde{I}_{i,j}(t)} - u(\widetilde{x},\widetilde{y},t)\right) - \frac{1}{|\widetilde{I}_{i,j}(t)|}\left(\widetilde{u}^{(\tilde p,\tilde q)}_{i,j} - \widetilde{u}_{i,j}\right) \end{aligned} \tag{2.29}$$

For $u^{\text{WENO}}_{(\tilde p,\tilde q)}(\widetilde{x},\widetilde{y})|_{\widetilde{I}_{i,j}(t)} - u(\widetilde{x},\widetilde{y},t)$, we have

$$\begin{aligned} &u^{\text{WENO}}_{(\tilde p,\tilde q)}(\widetilde{x},\widetilde{y})|_{\widetilde{I}_{i,j}(t)} - u(\widetilde{x},\widetilde{y},t)\\ =&\sum_{k=0}^{2}\left[\left(\widetilde{x}-x_{\tilde p}\right)\frac{\partial}{\partial x} + \left(\widetilde{y}-y_{\tilde q}\right)\frac{\partial}{\partial y}\right]^k \left(u^{\text{WENO}}_{(\tilde p,\tilde q)}(\cdot,\cdot) - u(\cdot,\cdot,t)\right)|_{(x_{\tilde p},y_{\tilde q})} + O(\Delta x^3). \end{aligned}$$

Following the same procedure in Remark A.1, we can easily prove that

$$\| D^\alpha \left(u^{\text{WENO}}_{(\tilde p,\tilde q)}(\cdot,\cdot) - u(\cdot,\cdot,t)\right)\|_\infty = O(\Delta x^{3-\alpha}) \tag{2.30}$$

Combining (2.30) with the fact that $\widetilde{x}-x_{\tilde p} = O(\Delta t)$, $\widetilde{y}-y_{\tilde q} = O(\Delta t)$, and $\Delta t\sim\Delta x\sim\Delta y$, we have

$$u^{\text{WENO}}_{(\tilde p,\tilde q)}(\widetilde{x},\widetilde{y})|_{\widetilde{I}_{i,j}(t)} - u(\widetilde{x},\widetilde{y},t) = O(\Delta x^3). \tag{2.31}$$

For $\frac{1}{|\widetilde{I}_{i,j}(t)|}\left(\widetilde{u}^{(\tilde p,\tilde q)}_{i,j} - \widetilde{u}_{i,j}\right)$,

$$
\begin{aligned}
&\frac{1}{|\widetilde{I}_{i,j}(t)|}\left(\widetilde{u}_{i,j}^{(\tilde{p},\tilde{q})}-\widetilde{u}_{i,j}\right)\\
=&\frac{1}{|\widetilde{I}_{i,j}(t)|}\left(\iint_{\widetilde{I}_{i,j}(t)} u^{\text{WENO}}_{(\tilde{p},\tilde{q})}(x,y)dxdy-\iint_{\widetilde{I}_{i,j}(t)} u^{\text{WENO}}(x,y)dxdy\right)\\
=&\frac{1}{|\widetilde{I}_{i,j}(t)|}\left(\iint_{\widetilde{I}_{i,j}(t)} \left(u^{\text{WENO}}_{(\tilde{p},\tilde{q})}(x,y)-u^{\text{WENO}}(x,y)\right)dxdy\right)
\end{aligned}
\tag{2.32}
$$

Since (2.31) is true for all $(\widetilde{x},\widetilde{y})\in\widetilde{I}_{i,j}(t)$ and

$$
u^{\text{WENO}}(x,y)-u(x,y,t)=O(\Delta x^3)\quad\text{for all }(x,y)\in\Omega \tag{2.33}
$$

from Remark A.1, we immediately have

$$
\frac{1}{|\widetilde{I}_{i,j}(t)|}\left(\widetilde{u}_{i,j}^{(\tilde{p},\tilde{q})}-\widetilde{u}_{i,j}\right)=O(\Delta x^3).\quad\square \tag{2.34}
$$

2.2.2. Approximation of the diffusion term

The strategy of constructing $\widetilde{\mathcal{G}}_{i,j}(\overline{\mathbf{U}};t)$ contains three steps. First, based on the finite volume information of u, we recover high-order finite volume information of Δu (assuming uniform mesh) by introducing a differential matrix. Second, we reconstruct a high-order piecewise polynomial to approximate Δu. Finally, we evaluate the corresponding integral over $\widetilde{I}_{i,j}(t)$ and obtain $\widetilde{\mathcal{G}}_{i,j}(\overline{\mathbf{U}};t)$. We emphasize here that the implicit treatment of the diffusion term is performed on the Eulerian mesh. This means that the differential matrix introduced in the following **Step 1** is necessary, as will be shown in Section 2.2.3. The details of these three steps are summarized as follows:

Step 1: *Recover high-order finite volume information of Δu.*
We recover

$$
\Delta\overline{\mathbf{U}}:=\mathbf{D}\overline{\mathbf{U}}, \tag{2.35}
$$

where $\mathbf{D}$ is the differential matrix assembled by the following local operators

$$
\overline{\Delta u}_{i,j}:=\left[-\frac{1}{12}\ \ \frac{4}{3}\ \ -\frac{5}{2}\ \ \frac{4}{3}\ \ -\frac{1}{12}\right]\left(\frac{1}{\Delta x^2}\begin{bmatrix}\overline{u}_{i-2,j}\\ \overline{u}_{i-1,j}\\ \overline{u}_{i,j}\\ \overline{u}_{i+1,j}\\ \overline{u}_{i+2,j}\end{bmatrix}+\frac{1}{\Delta y^2}\begin{bmatrix}\overline{u}_{i,j-2}\\ \overline{u}_{i,j-1}\\ \overline{u}_{i,j}\\ \overline{u}_{i,j+1}\\ \overline{u}_{i,j+2}\end{bmatrix}\right),
$$

for all i,j, and corresponding boundary conditions.

Step 2: *Recover a piecewise reconstruction polynomial of Δu.*
We utilize the same polynomial $q_0(x,y)$ in Appendix A as the reconstruction formula and denote the final piecewise polynomial by $\Delta u^{\text{rec}}(x,y)$.

Step 3: *Compute the integral of $\Delta u^{\text{rec}}(x,y)$ as the final approximation.*

$$
\begin{aligned}
&\widetilde{\mathcal{G}}_{i,j}(\overline{\mathbf{U}};t)\\
=&\epsilon\iint_{\widetilde{I}_{i,j}(t)}\Delta u\,dxdy\approx\epsilon\iint_{\widetilde{I}_{i,j}(t)}\Delta u^{\text{rec}}(x,y)dxdy:=\epsilon\widetilde{\Delta u}_{i,j}\left(\overline{\mathbf{U}};t\right)\quad\text{for all }\ i,j,
\end{aligned}
\tag{2.36}
$$

where the integral of piecewise polynomial is accomplished by the method of our previous work [44].

2.2.3. High-order IMEX RK temporal discretization

In light of the high-order spatial discretization presented in (2.8), (2.23), and (2.36), we introduce the IMEX RK temporal discretizations. Under the IMEX setting, we evolve the convection flux term explicitly while evolving the diffusion term implicitly. In addition, the time-step constraint is controlled by the explicit convection part, with $\Delta t\sim\sqrt{\min\{\Delta x,\Delta y\}}$.

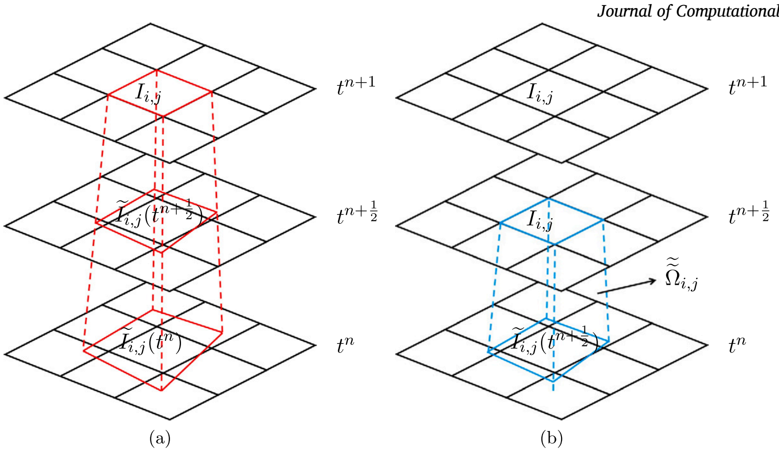

Fig. 2.3. Schematic illustration of full discretization with IMEX(1,2,2).

An IMEX RK scheme can be represented by the following two butcher tables [3]:

Implicit Scheme

$$\begin{array}{c|ccccc} 0 & 0 & 0 & 0 & \cdots & 0 \\ c_1 & 0 & a_{11} & 0 & \cdots & 0 \\ c_2 & 0 & a_{21} & a_{22} & \cdots & 0 \\ \vdots & \vdots & \vdots & \vdots & \ddots & \vdots \\ c_s & 0 & a_{s1} & a_{s2} & \cdots & a_{ss} \\ \hline & 0 & b_1 & b_2 & \cdots & b_s \end{array}$$

Explicit Scheme

$$\begin{array}{c|ccccc} 0 & 0 & 0 & 0 & \cdots & 0 \\ c_1 & \hat{a}_{21} & 0 & 0 & \cdots & 0 \\ c_2 & \hat{a}_{31} & \hat{a}_{32} & 0 & \cdots & 0 \\ \vdots & \vdots & \vdots & \vdots & \ddots & \vdots \\ c_{\sigma-1} & \hat{a}_{\sigma,1} & \hat{a}_{\sigma,2} & \hat{a}_{\sigma,3} & \cdots & 0 \\ \hline & \hat{b}_1 & \hat{b}_2 & \hat{b}_3 & \cdots & \hat{b}_\sigma \end{array}$$

A triplet (s, σ, p) is used to demonstrate that the IMEX scheme uses an s-stage implicit scheme and a σ-stage explicit scheme achieving pth-order accuracy.

The butcher table of first-order IMEX scheme in (2.11), which is also called IMEX(1,1,1) in [3], is

Implicit Scheme

$$\begin{array}{c|cc} 0 & 0 & 0 \\ 1 & 0 & 1 \\ \hline & 0 & 1 \end{array}$$

Explicit Scheme

$$\begin{array}{c|cc} 0 & 0 & 0 \\ 1 & 1 & 0 \\ \hline & 1 & 0 \end{array}$$

The second-order IMEX(1,2,2) scheme in [3] is represented by the following butcher tables:

Implicit Scheme

$$\begin{array}{c|cc} 0 & 0 & 0 \\ \frac{1}{2} & 0 & \frac{1}{2} \\ \hline & 0 & 1 \end{array}$$

Explicit Scheme

$$\begin{array}{c|cc} 0 & 0 & 0 \\ \frac{1}{2} & \frac{1}{2} & 0 \\ \hline & 0 & 1 \end{array}$$

One noteworthy complexity of IMEX(1,2,2), in contrast to IMEX(1,1,1), is its involvement of the intermediate time level $t^{n+\frac{1}{2}}$ (see Fig. 2.3a). To construct a full discretization based on IMEX(1,2,2), we define a new characteristic region $\widetilde{\widetilde{\Omega}}_{i,j} := \{(x,y,t)|(x,y) \in \widetilde{I}_{i,j}(t+\frac{1}{2}\Delta t),\ \ t \in [t^n, t^{n+\frac{1}{2}}]\}$ for each mesh index (i,j) (see Fig. 2.3b), following a similar strategy as proposed in [32]. For $\{\widetilde{\widetilde{\Omega}}_{i,j}\}$, we define an operator $\widetilde{\widetilde{\mathcal{W}}}$ such that $\widetilde{\widetilde{\mathcal{W}}}(\overline{\mathbf{U}}, t^{n+\alpha})$ represents the corresponding WENO piecewise polynomial with respect to $\{\widetilde{I}_{i,j}(t^{n+\frac{1}{2}+\alpha})\}$, which is constructed based on $\overline{\mathbf{U}}$. Furthermore, we define that $\widetilde{\widetilde{\mathcal{F}}}(\overline{\mathbf{U}}, t^{n+\alpha}) := \left(\widetilde{\widetilde{\mathcal{F}}}_{i,j}(\overline{\mathbf{U}}, t^{n+\alpha})\right)_{N_x N_y}$ with

$$\widetilde{\widetilde{\mathcal{F}}}_{i,j}(\overline{\mathbf{U}}, t^{n+\alpha}) := -\int_{\partial \widetilde{I}_{i,j}(t^{n+\frac{1}{2}+\alpha})} \hat{F}(\widetilde{\widetilde{\mathcal{W}}}(\overline{\mathbf{U}}, t^{n+\alpha}), x, y, t^{n+\alpha}) ds, \quad \text{for all } \ i,j. \tag{2.37}$$

Then, the second-order fully discrete scheme is provided as follows (see Fig. 2.3):

$$\mathbf{M}\overline{\mathbf{U}}^{(1)} = \widetilde{\widetilde{\mathbf{U}}}^n + \frac{1}{2}\Delta t \widetilde{\widetilde{\mathcal{F}}}(\overline{\mathbf{U}}^n, t^n) + \frac{1}{2}\Delta t \left(\epsilon \mathbf{M}\mathbf{D}\overline{\mathbf{U}}^{(1)}\right), \tag{2.38}$$

$$\mathbf{M}\overline{\mathbf{U}}^{n+1} = \widetilde{\mathbf{U}}^n + \Delta t\widetilde{\mathcal{F}}(\overline{\mathbf{U}}^{(1)}, t^{n+\frac{1}{2}}) + \Delta t\widetilde{\mathcal{G}}(\overline{\mathbf{U}}^{(1)}, t^{n+\frac{1}{2}}), \tag{2.39}$$

where

- the notation $\widetilde{\widetilde{\cdot}}$ is used to indicate that the corresponding values or operations refer to specific slices of the characteristic region $\widetilde{\widetilde{\Omega}}_{i,j}$,
- $\widetilde{\widetilde{\mathbf{U}}}^n =: \left(\iint_{\widetilde{I}_{i,j}(t^{n+\frac{1}{2}})} \mathcal{W}\left(\overline{\mathbf{U}}^n\right) dxdy\right)_{N_x N_y}$ (see Fig. 2.3b).

The design of the additional characteristic region $\widetilde{\widetilde{\Omega}}_{i,j}$ helps us avoid the expansive reconstruction procedure associated with nonuniform Lagrangian meshes at the intermediate time level, which dynamically change as time evolves. For the numerical tests, we employ IMEX(2,3,3) as described in [3] to construct a third-order fully discretized EL-RK-FV-WENO-IMEX scheme. We omit the details for IMEX(2,3,3) since the key techniques have already been covered in the IMEX(1,2,2) case.

2.3. EL-RK-FV-WENO scheme for the nonlinear convection-diffusion equation

Consider

$$u_t + (f_1(u))_x + (f_2(u))_y = \epsilon(u_{xx} + u_{yy}). \tag{2.40}$$

To extend the proposed scheme for (2.40), we further design two modifications with very limited extra cost. The two modifications utilize the EL-RK-FV framework designed in the previous sections and no longer require the adoption of one temporal method within another as in [12]. We summarize the details of these two modifications as follows:

1. *Redesign the modified velocity field.*
The construction of the original modified velocity field requires the exact velocity field at $t = t^{n+1}$, which is unknown for nonlinear models. We redesign that $(\alpha(x, y, t), \beta(x, y, t))$ is defined by first applying interpolation at $t = t^{n+1}$ such that

$$\begin{aligned}\alpha(x_{i\pm\frac{1}{2}}, y_{j\pm\frac{1}{2}}, t^{n+1}) &= f_1'(\mathcal{W}(\overline{\mathbf{U}}^n))|_{(x_{i\pm\frac{1}{2}}, y_{j\pm\frac{1}{2}})},\\ \beta(x_{i\pm\frac{1}{2}}, y_{j\pm\frac{1}{2}}, t^{n+1}) &= f_2'(\mathcal{W}(\overline{\mathbf{U}}^n))|_{(x_{i\pm\frac{1}{2}}, y_{j\pm\frac{1}{2}})},\end{aligned} \tag{2.41}$$

and then following the same procedure as in (2.3)-(2.5). This modified velocity field can still give us the same time-step constraint $\Delta t \sim \sqrt{\min\{\Delta x, \Delta y\}}$ if we apply similar analysis as in Remark 2.1. This flexibility of defining the modified velocity field is of vital importance. In our previous semi-Lagrangian work for convection-diffusion equations [20], the necessity of an exact velocity field presents challenges in adapting the approach for nonlinear models.
2. *Recover the velocity fields at intermediate time levels.*
The velocity field for $t \in (t^n, t^{n+1}]$, which is required for evaluating numerical fluxes, is unknown for nonlinear models. For this issue, we simply use the predicted solutions at the intermediate time levels to recover corresponding velocity fields. For example, in (2.39), the exact velocity field $(a(x, y, t^{n+\frac{1}{2}}), b(x, y, t^{n+\frac{1}{2}}))$ is replaced with $\left(f_1'(\mathcal{W}(\overline{\mathbf{U}}^{(1)})), f_2'(\mathcal{W}(\overline{\mathbf{U}}^{(1)}))\right)$ for $\widetilde{\mathcal{F}}\left(\overline{\mathbf{U}}^{(1)}, t^{n+\frac{1}{2}}\right)$.

3. Numerical tests

In this section, we apply the proposed EL-RK-FV-WENO scheme to four challenging problems. The first two problems involve linear equations: the swirling deformation flow, characterized by pure convection terms, and the 0D2V Leonard-Bernstein linearized Fokker-Planck equation. The latter two are nonlinear models: the Kelvin-Helmholtz instability problem, again with pure convection terms, and the incompressible Navier-Stokes equations. We use these four cases to demonstrate the effectiveness and the designed properties of the proposed scheme. The time-steps in the following are defined by:

$$\Delta t = \frac{\text{CFL}}{\frac{\max\{|f'(u)|\}}{\Delta x} + \frac{\max\{|g'(u)|\}}{\Delta y}}, \tag{3.1}$$

where $\left(f'(u), g'(u)\right)$ represents the corresponding velocity field. For pure convection simulation, we use the third-order Runge-Kutta temporal discretization with the following butcher table:

$$\begin{array}{c|ccc} 0 & 0 & 0 & 0 \\ \frac{1}{2} & \frac{1}{2} & 0 & 0 \\ 1 & -1 & 2 & 0 \\ \hline & \frac{1}{6} & \frac{2}{3} & \frac{1}{6} \end{array}$$

Table 3.1
(Swirling deformation flow) L^1, L^2, and L^∞ errors and corresponding orders of accuracy of the EL-RK-FV-WENO scheme for (3.2) with initial condition (3.3) at $t = 1.5$ with CFL = 1.

mesh	L^1 error	order	L^2 error	order	L^∞ error	order
100× 100	7.28E-04	—	4.98E-03	—	1.05E-01	—
200× 200	1.19E-04	2.62	8.00E-04	2.64	1.73E-02	2.59
300× 300	3.64E-05	2.91	2.46E-04	2.91	5.70E-03	2.74
400× 400	1.55E-05	2.97	1.05E-04	2.96	2.67E-03	2.64

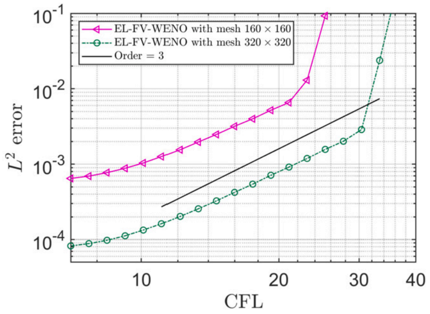

Fig. 3.4. (Swirling deformation flow) Log-log plot of CFL numbers versus L^2 errors with fixed meshes 160×160 and 320×320 at $t = 1.5$ of the EL-RK-FV-WENO scheme.

For convection-diffusion simulation, we apply IMEX(2,3,3) in [3] with the following butcher tables:

Implicit Scheme

$$\begin{array}{c|ccc} 0 & 0 & 0 & 0 \\ \gamma & 0 & \gamma & 0 \\ 1-\gamma & 0 & 1-2\gamma & \gamma \\ \hline & 0 & \frac{1}{2} & \frac{1}{2} \end{array}$$

Explicit Scheme

$$\begin{array}{c|ccc} 0 & 0 & 0 & 0 \\ \gamma & \gamma & 0 & 0 \\ 1-\gamma & \gamma-1 & 2(1-\gamma) & 0 \\ \hline & 0 & \frac{1}{2} & \frac{1}{2} \end{array}$$

where $\gamma = (3 + \sqrt{3})/6$.

3.1. Linear models

Example 3.1. (Swirling deformation flow). Consider the following equation:

$$u_t - (2\pi\cos^2(\frac{x}{2})\sin(y)g(t)u)_x + (2\pi\sin(x)\cos^2(\frac{y}{2})g(t)u)_y = 0, \quad x,\ y \in [-\pi, \pi], \tag{3.2}$$

where $g(t) = \cos(\pi t/T)$ with $T = 1.5$. We first consider (3.2) with the following smooth initial condition:

$$u(x, y, 0) = \begin{cases} r_0^b \cos(\frac{r^b(\mathbf{x})\pi}{2r_0^b})^6 & \text{if } r^b(\mathbf{x}) < r_0^b, \\ 0, & \text{otherwise}, \end{cases} \tag{3.3}$$

where $r_0^b = 0.3\pi$, $r^b(\mathbf{x}) = \sqrt{(x - x_0^b)^2 + (y - y_0^b)^2}$ and the center of the cosine bell $(x_0^b, y_0^b) = (0.3\pi, 0)$. Table 3.1 shows the L^1, L^2, and L^∞ errors and corresponding orders of accuracy for the proposed scheme. As indicated, the expected 3rd-order spatial accuracy is achieved through mesh refinement.

In Fig. 3.4, by varying the CFL number while fixing the spatial mesh, we investigate the temporal order of accuracy. For the results using mesh 160×160, the proposed scheme demonstrates 3rd-order temporal accuracy and is stable when CFL is less than 21. For the mesh 320×320, stability is observed at least up to CFL = 30, corroborating our time-step constraint estimate (2.18).

To validate the essentially non-oscillatory nature of the proposed WENO reconstruction, we consider a discontinuous initial condition featuring a cylinder with a notch, a cone, and a smooth bell as shown in Fig. 3.5. Fig. 3.6 display the mesh plots of the numerical solutions at $t = 0.75$ (left) and $t = 1.5$ (right). The swirling deformation flow significantly deforms the solution at half the period ($t = 0.75$) and then reforms it back to its initial state at $t = 1.5$. On the left side of Fig. 3.7, we test the proposed scheme using our previous WENO-ZQ reconstruction from [44] and observe small numerical oscillations. On the right side of Fig. 3.7, we present the cross-sections of the numerical solutions of the EL-RK-FV scheme equipped with both the new WENO-ZQ reconstruction and our previous WENO-ZQ from [44]. The results indicate that the new WENO-ZQ reconstruction performs better in controlling numerical oscillations.

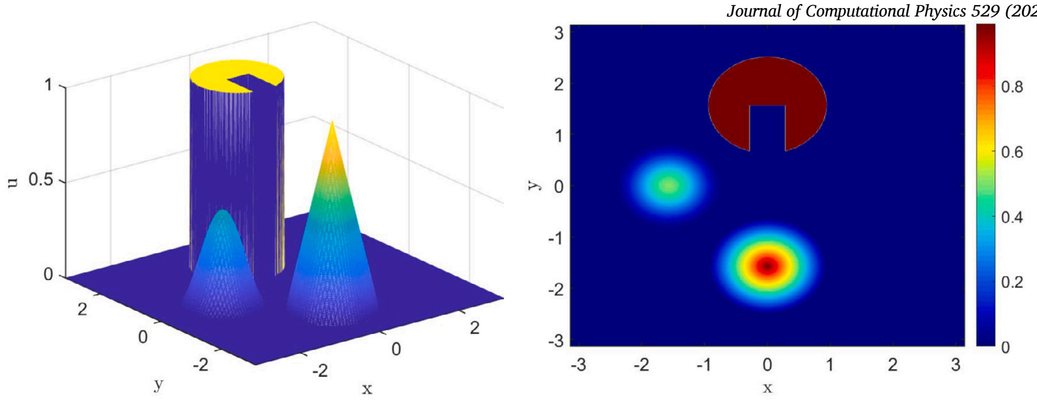

(a) Mesh plot (b) Contour plot

Fig. 3.5. (Swirling deformation flow) Mesh plot and contour plot of a discontinuous initial condition.

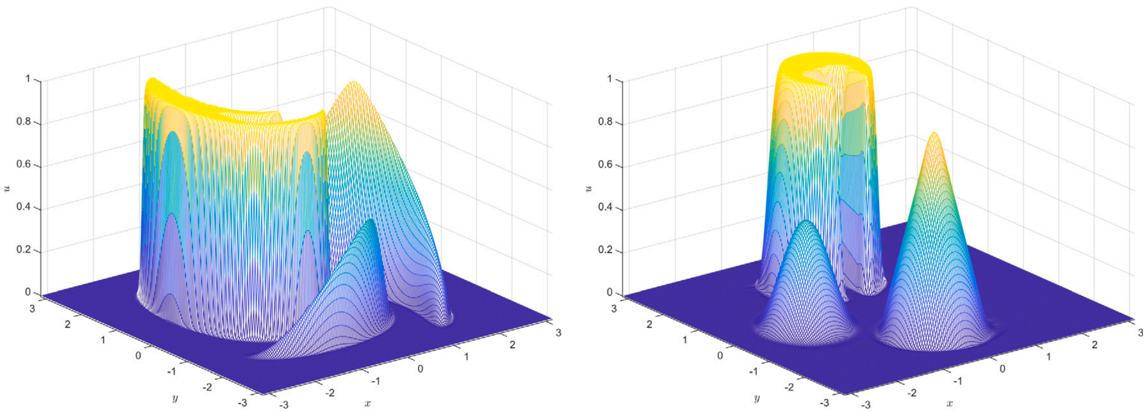

(a) $t = 0.75$ (b) $t = 1.5$

Fig. 3.6. (Swirling deformation flow) Mesh plot and contour plot of the numerical solution of the EL-RK-FV-WENO scheme with CFL $= 10.2$ and mesh size 200×200 at $t = 0.75$ (left) and at $t = 1.5$ (right).

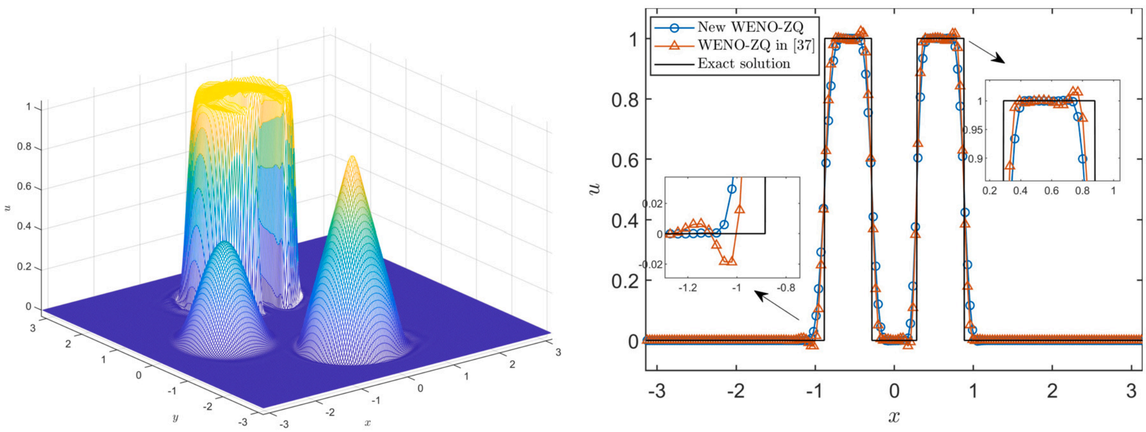

Fig. 3.7. (Swirling deformation flow) Left: Mesh plot of the numerical solution of the EL-RK-FV scheme using the WENO-ZQ reconstruction in [44] with CFL $= 10.2$ and mesh size 200×200 at $t = 1.5$. Right: Cross-sections of the numerical solutions of the EL-RK-FV scheme equipped with the new WENO-ZQ reconstruction and our previous WENO-ZQ in [44] with CFL $= 10.2$ and mesh size 200×200 at $t = 1.5$ and $y \approx 2.04$.

In summary, this example illustrates the effectiveness of the proposed EL-RK-FV evolving strategy for the convection terms. This strategy, which involves remapping from Eulerian to Lagrangian spatial approximations, not only achieves high-order spatial and temporal accuracy but also allows for large time-steps while maintaining a non-oscillatory property.

Table 3.2
(The 0D2V Leonard-Bernstein linearized Fokker-Planck equation) L^1, L^2, and L^∞ errors and corresponding orders of accuracy of the EL-RK-FV-WENO scheme for (3.4) with initial condition (3.5) at $t = 0.5$ with CFL = 1.

mesh	L^1 error	order	L^2 error	order	L^∞ error	order
20× 20	2.18E-03	—	1.38E-02	—	2.95E-01	—
40× 40	3.01E-04	2.85	2.05E-03	2.75	9.50E-02	1.63
80× 80	3.33E-05	3.18	1.58E-04	3.70	6.40E-03	3.89
160× 160	4.10E-06	3.02	1.80E-05	3.13	2.88E-04	4.47
320× 320	4.77E-07	3.10	2.10E-06	3.11	3.20E-05	3.17

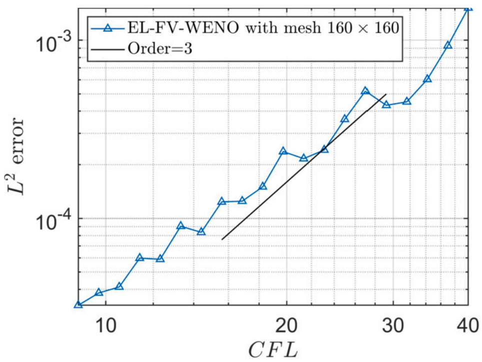

Fig. 3.8. (The 0D2V Leonard-Bernstein linearized Fokker-Planck equation) Log-log plot of CFL numbers versus L^2 errors with fixed mesh 160×160 at $t = 0.5$ for the EL-RK-FV-WENO scheme.

Table 3.3
(The 0D2V Leonard-Bernstein linearized Fokker-Planck equation) Settings of the Maxwellians f_{M1} and f_{M2}.

	f_{M1}	f_{M2}
n	1.990964530353041	1.150628123236752
$\bar{v}_x$	0.4979792385268875	-0.8616676237412346
$\bar{v}_y$	0	0
T	2.46518981703837	0.4107062104302872

Example 3.2. (The 0D2V Leonard-Bernstein linearized Fokker-Planck equation) Consider the following equation:

$$f_t + \frac{1}{\epsilon}\left((v_x - \bar{v}_x)f\right)_{v_x} - \frac{1}{\epsilon}\left((v_y - \bar{v}_y)f\right)_{v_y} = \frac{1}{\epsilon} D\left(f_{v_x v_x} + f_{v_y v_y}\right), \quad v_x, v_y \in [-2\pi, 2\pi] \tag{3.4}$$

with zero boundary conditions and an equilibrium solution by the given Maxwellian:

$$f_M(v_x, v_y) = \frac{n}{2\pi RT} \exp\left(\frac{(v_x - \bar{v}_x)^2 + (v_y - \bar{v}_y)^2}{2RT}\right), \tag{3.5}$$

where, $\epsilon = 1$, gas constant $R = 1/6$, temperature $T = 3$, thermal velocity $v_{th} = \sqrt{2RT} = \sqrt{2D} = 1$, number density $n = \pi$, and bulk velocities $\bar{v}_x = \bar{v}_y = 0$. For spatial and temporal accuracy tests, we choose $f(v_x, v_y, 0) = f_M(v_x, v_y)$. In Table 3.2, we present the L^1, L^2, and L^∞ errors and the corresponding orders of accuracy for the proposed scheme. The results demonstrate a consistent 3rd-order spatial accuracy.

By fixing the spatial mesh and varying the CFL number, the temporal order of accuracy is investigated in Fig. 3.8. The proposed scheme exhibits 3rd-order temporal accuracy and allows the use of large time-steps, as evidenced by the stability for high CFL numbers.

To test the relaxation of the system, we choose the initial condition $f(v_x, v_y, t = 0) = f_{M1}(v_x, v_y) + f_{M2}(v_x, v_y)$, where the parameters of each Maxwellian, f_{M1} and f_{M2}, are detailed in Table 3.3. The two Maxwellians are shifted along the v_x direction with $\bar{v}_y = 0$. The evolution of the numerical results, illustrated in Fig. 3.9, shows that after $t \geq 3$, there is no discernible difference between the numerical solution and the solution at $t = 3$, validating the efficacy of the proposed scheme.

In Fig. 3.10, we present the capability of the proposed scheme in preserving various physical conservative quantities. The results indicate that while the scheme is effective in conserving mass, it does not maintain the other quantities to the machine precision.

To encapsulate, this example primarily demonstrates the effectiveness of the IMEX temporal discretization, which combines the implicit solver for the diffusion term and the EL evolving strategy for the convection terms, enabling the use of large time-steps.

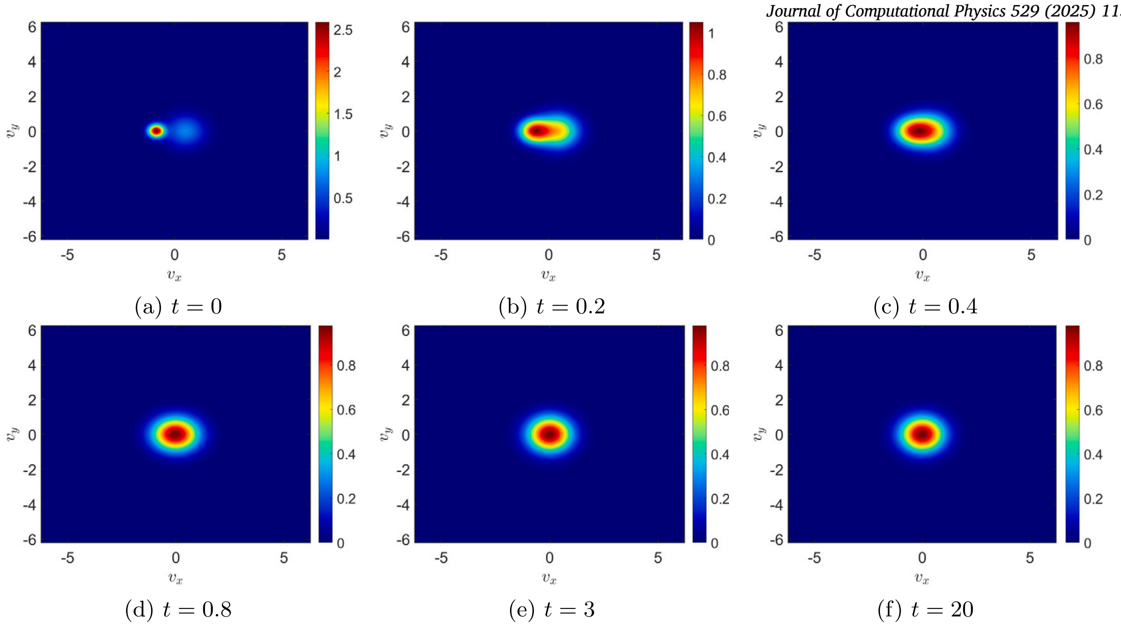

Fig. 3.9. (The 0D2V Leonard-Bernstein linearized Fokker-Planck equation) Contour plots of the numerical results of the EL-RK-FV-WENO scheme with CFL $= 3$ and mesh size 100×100 at $t = 0$ (initial condition), $t = 0.2$, $t = 0.4$, $t = 0.6$, $t = 3$, and $t = 20$.

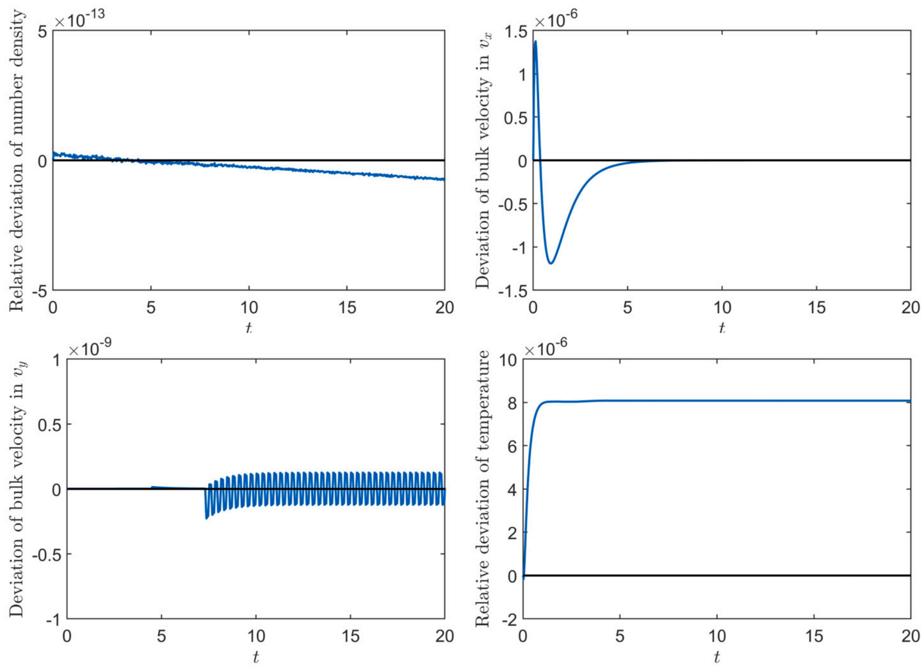

Fig. 3.10. (The 0D2V Leonard-Bernstein linearized Fokker-Planck equation) Relative deviation (or deviation) of number density, bulk velocity in v_x, bulk velocity in v_y, and temperature for the EL-RK-FV-WENO scheme with CFL $= 10.2$ and with mesh 160×160 from $t = 0$ to $t = 20$.

3.2. Nonlinear models

Example 3.3. (Kelvin-Helmholtz instability problem) Consider the guiding center Vlasov model [33,19]:

$$\begin{aligned} &\rho_t + \nabla \cdot (\mathbf{E}^{\perp} \rho) = 0, \\ -&\Delta \Phi = \rho, \quad \mathbf{E}^{\perp} = \left(-\Phi_y, \Phi_x\right), \end{aligned} \tag{3.6}$$

with the periodic boundary condition and the following initial condition:

Table 3.4
(Kelvin-Helmholtz instability problem) L^1, L^2, and L^∞ errors and corresponding orders of accuracy of the EL-RK-FV-WENO scheme for (3.6) with initial condition (3.7) at $t = 5$ with CFL = 1.

mesh	L^1 error	order	L^2 error	order	L^∞ error	order
16× 16	6.79E-03	—	1.11E-02	—	6.68E-02	—
32× 32	5.48E-04	3.63	9.46E-04	3.55	1.18E-02	2.50
64× 64	4.35E-05	3.66	7.15E-05	3.73	1.43E-03	3.05
128× 128	4.37E-06	3.31	6.45E-06	3.47	1.98E-04	2.85
256× 256	5.23E-07	3.06	6.72E-07	3.26	1.73E-05	3.51

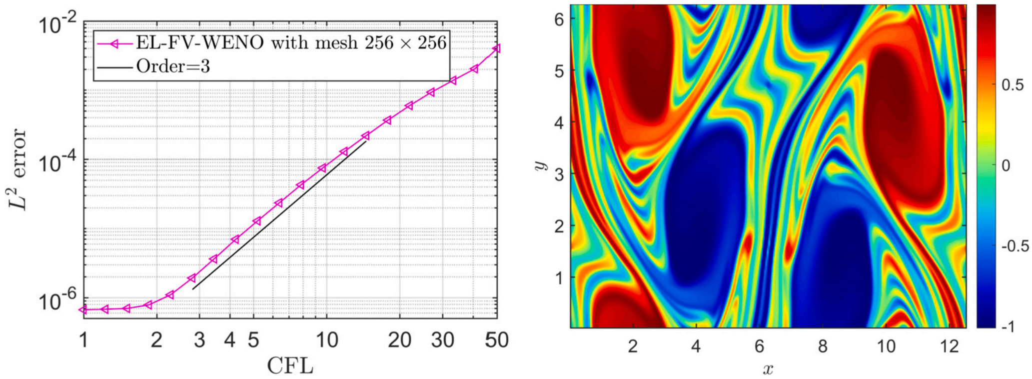

Fig. 3.11. (Kelvin-Helmholtz instability problem) Left: Log-log plot of CFL numbers versus L^2 errors with fixed mesh 256×256 at $t = 5$ of the EL-RK-FV-WENO scheme. Right: Contour plot of the numerical solution of the EL-RK-FV-WENO scheme with CFL = 10.2 and with mesh 256×256 at $t = 40$.

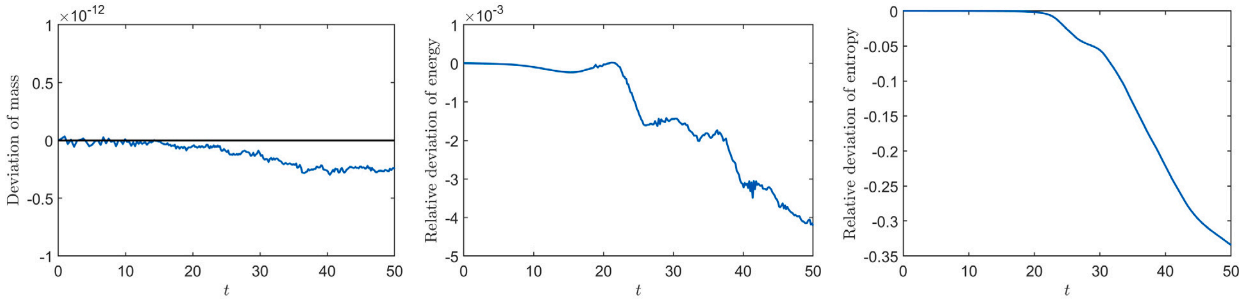

(a) Deviation of mass (b) Relative deviation of energy (c) Relative deviation of entropy

Fig. 3.12. (Kelvin-Helmholtz instability problem) Deviation of mass, relative deviation of energy and entropy for the EL-RK-FV-WENO scheme with CFL = 10.2 and with mesh 256×256 from $t = 0$ to $t = 50$.

$$\rho(x, y, 0) = \sin(y) + 0.015\cos(0.5x), \quad x \in [0, 4\pi], \quad y \in [0, 2\pi], \tag{3.7}$$

where ρ is the charge density and $\mathbf{E}$ is the electric field. The Poisson's equation in (3.6) is solved using a Fast Fourier Transform (FFT) solver, with reconstructions facilitating the exchange of nodal and modal information [44]. We validate the 3rd-order spatial and temporal accuracy of the proposed scheme in Table 3.4 and on the left side of Fig. 3.11. Additionally, the stability of the scheme with large time-steps up to CFL = 50 is verified.

On the right side of Fig. 3.11, we display the contour plot of the numerical solution of the EL-RK-FV-WENO scheme at $t = 40$. The result is comparable with the one of our fourth-order SL-FV-WENO scheme in [44].

In Fig. 3.12, we show the deviation of mass, relative deviation of energy and entropy of the proposed scheme from $t = 0$ to $t = 50$. As shown, the proposed scheme is mass conservative. The magnitudes of relative deviation of energy and entropy results are comparable with the ones in [44].

This nonlinear example effectively showcases the success of the generalization strategy for nonlinear model outlined in Section 2.3, which is achieved with minimal additional cost.

Example 3.4. (Incompressible Navier-Stokes equations) The governing equations are as follows:

$$\begin{aligned} &\omega_t + (u\omega)_x + (v\omega)_y = \nu(\omega_{xx} + \omega_{yy}), \\ &\qquad \Delta\psi = \omega, \quad (u, v) = \left(\psi_y, \psi_x\right), \end{aligned} \tag{3.8}$$

Table 3.5
(Incompressible Navier-Stokes equations) L^1, L^2, and L^∞ errors and corresponding orders of accuracy of the EL-RK-FV-WENO scheme for (3.8) with initial condition (3.9) at $t = 0.5$ with CFL = 1.

mesh	L^1 error	order	L^2 error	order	L^∞ error	order
16× 16	3.90E-03	—	4.65E-03	—	1.14E-02	—
32× 32	4.88E-04	3.00	5.82E-04	3.00	1.45E-03	2.98
64× 64	6.09E-05	3.00	7.27E-05	3.00	1.82E-04	2.99
128× 128	7.61E-06	3.00	9.08E-06	3.00	2.29E-05	2.99
256× 256	9.51E-07	3.00	1.13E-06	3.00	2.86E-06	3.00

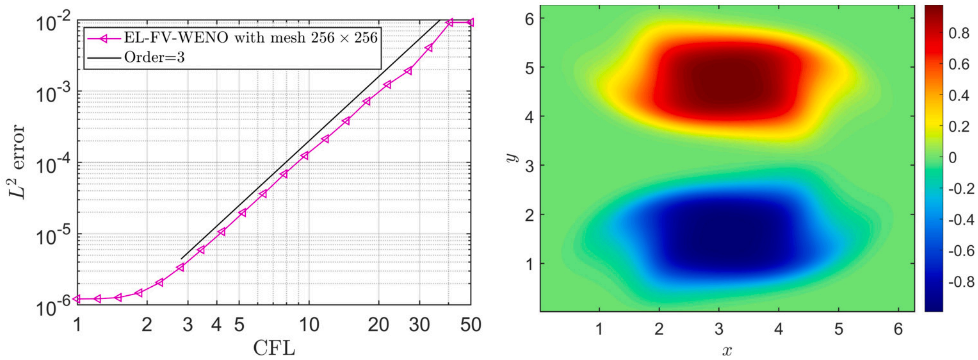

Fig. 3.13. (Incompressible Navier-Stokes equations) Left: log-log plot of CFL numbers versus L^2 errors with fixed mesh 256×256 at $t = 0.5$ of the EL-RK-FV-WENO scheme. Right: contour plot of the numerical solution of the EL-RK-FV-WENO scheme for the vortex patch problem with CFL = 10.2 and with mesh 256×256 at $t = 5$.

where ω is the vorticity of the flow, (u, v) is the velocity field, and ν is the kinematic viscosity, which is set to be $\frac{1}{100}$. We first consider an initial condition given by:

$$\omega(x, y, 0) = -2\sin(x)\sin(y), \quad x \in [0, 2\pi], \quad y \in [0, 2\pi] \tag{3.9}$$

with the exact solution $\omega(x, y, t) = -2\sin(x)\sin(y)\exp(-2t\nu)$. Similarly, 3rd-order spatial and temporal order of accuracy of validated in Table 3.5 and on the left side of Fig. 3.13 respectively. For this problem, we observe that large time-steps are allowed for the proposed scheme up to CFL = 40.

For a more complex scenario, we consider the incompressible Navier-Stokes equation (3.8) on $[0, 2\pi]^2$ with the following initial condition (the vortex patch problem)

$$\omega(x, y, 0) = \begin{cases} -1, & \frac{\pi}{2} \le x \le \frac{3\pi}{2}, \quad \frac{\pi}{4} \le y \le \frac{3\pi}{4}; \\ 1, & \frac{\pi}{2} \le x \le \frac{3\pi}{2}, \quad \frac{5\pi}{4} \le y \le \frac{7\pi}{4}; \\ 0 & \text{otherwise} \end{cases} \tag{3.10}$$

with zero boundary condition. We show the contour plot of the numerical solution of the proposed scheme at $t = 5$ on the right side of Fig. 3.13. The numerical result on the right of Fig. 3.13 is comparable with the one in [41].

Reflecting on this example, we note that the proposed EL-RK-FV-WENO scheme is able to simulate a nonlinear convection-diffusion equation with all the designed good properties. This is one of the major reasons why this EL-RK-FV-WENO scheme is attractive compared with our previous SL-FV-WENO scheme [44].

4. Conclusion

In this paper, we introduce a high-order EL-RK-FV-WENO scheme for nonlinear convection-diffusion equations. By defining a modified velocity field and corresponding flux-form semi-discretization, the scheme relaxes the time-step constraint. To ensure mass conservation, high order accuracy in both space and time, and high resolution for discontinuous solutions, while enabling explicitly large time-stepping sizes, the spatial discretization is designed to align with the EL formulation and surmount the challenges posed by the modified velocity field. In this paper, we introduce a scheme with spatial-temporal third-order convergence. Theoretically, a straightforward extension to the fourth order is possible and will be the focus of our future research. It is well known that proposing a robust and essentially non-oscillatory scheme for the transport of discontinuous solutions is far from trivial. To address this challenge, we propose an improved WENO scheme. Compared with the SL-FV scheme in [44], the proposed EL-RK-FV-WENO scheme is capable of simulating nonlinear convection-diffusion equations while inheriting the ability to apply large time-steps. Extensive numerical tests, ranging from the linear convection-diffusion equation and the Navier-Stokes equations to their zero-diffusive limit (nonlinear Euler equations), are conducted, verifying the effectiveness of the proposed scheme.

CRediT authorship contribution statement

Nanyi Zheng: Writing – review & editing, Writing – original draft, Visualization, Validation, Software, Methodology, Investigation, Formal analysis, Conceptualization. **Xiaofeng Cai:** Writing – review & editing, Writing – original draft, Validation, Methodology, Funding acquisition, Conceptualization. **Jing-Mei Qiu:** Writing – review & editing, Validation, Supervision, Resources, Project administration, Methodology, Investigation, Funding acquisition, Conceptualization. **Jianxian Qiu:** Writing – review & editing, Validation, Supervision, Methodology, Funding acquisition, Conceptualization.

Declaration of competing interest

The authors declared that they have no conflicts of interest to this work. We declare that we do not have any commercial or associative interest that represents a conflict of interest in connection with the work submitted.

Acknowledgements

The research of the fourth author was partially supported by National Key R&D Program of China (No. 2022YFA1004500); the work of the first and third authors were supported by the National Science Foundation NSF-DMS-2111253, Air Force Office of Scientific Research FA9550-22-1-0390, the Department of Energy DE-SC0023164 and the Air Force Office of Scientific Research (AFOSR) FA9550-24-1-0254 via the Multidisciplinary University Research Initiatives (MURI) Program; the work of the second author was supported by the National Natural Science Foundation of China (No. 12201052), the Guangdong Provincial Key Laboratory of Interdisciplinary Research and Application for Data Science, BNU-HKBU United International College, project code 2022B1212010006, National Key Laboratory for Computaional Physics [6142A05230201].

Appendix A. Third-order WENO-ZQ reconstruction method for Eulerian mesh

In this appendix, we introduce the 3rd-order WENO-ZQ reconstruction for the Eulerian mesh. For convenience, we assume $\Delta x_i \equiv \Delta x$ and $\Delta y_j \equiv \Delta y$ for all $i,\ j$. We define $\mu_i(x) := \frac{x-x_i}{\Delta x}$, $\nu_j(y) := \frac{y-y_j}{\Delta y}$ and introduce a set of local orthogonal polynomials as $\{P_l^{(i,j)}(x,y)\}$ for a given cell $I_{i,j}$:

$$\begin{aligned} &P_1^{(i,j)} := 1, \quad P_2^{(i,j)} := \mu_i(x), \quad P_3^{(i,j)} := \nu_j(y), \\ &P_4^{(i,j)} := \mu_i^2(x) - \frac{1}{12}, \quad P_5^{(i,j)} := \mu_i(x)\nu_j(y), \quad P_6^{(i,j)} := \nu_j^2(y) - \frac{1}{12}. \end{aligned} \tag{A.1}$$

We assume that $\overline{u}_5 := \overline{u}_{i,j}$ and $I_5 := I_{i,j}$, while $\{u_s\}$ and $\{I_s\}$ represent corresponding cell averages and Eulerian cells based on the serial number in Fig. A.14. The reconstruction procedure is performed as follows:

Step 1 Construct a quadratic polynomial $q_0(x,y) = \sum_{l=1}^{6} a_l^{q_0} P_l^{(i,j)}(x,y)$ using a special least-squares procedure. We define

$$V := \{p(x,y) \in P^2(I_{i,j}) | \frac{1}{\Delta x \Delta y} \int_{I_s} p(x,y)dxdy = \overline{u}_s,\ s = 2,4,5,6,8\},$$

$$E(p(x,y)) := \left[\sum_{s=1,3,7,9} \left(\frac{1}{\Delta x \Delta y} \int_{I_s} p(x,y)dxdy - \overline{u}_s \right)^2 \right]^{\frac{1}{2}}.$$

Then, we determine that $q_0(x,y)$ is the unique polynomial satisfying:

$$E(q_0(x,y)) = \min_{p \in V} E(p(x,y)). \tag{A.2}$$

Step 2 Construct eight linear polynomials $\{q_k(x,y)\}_{k=1}^{8} = \{\sum_{l=1}^{3} a_l^{q_k} P_l^{(i,j)}(x,y)\}$ satisfying:

$$\frac{1}{\Delta x \Delta y} \iint_{I_5} q_k(x,y)dxdy = \overline{u}_5 \quad \text{for} \quad k = 1,2,\ldots,8, \tag{A.3}$$

and

$$\frac{1}{\Delta x \Delta y} \iint_{I_s} q_k(x,y)dxdy = \overline{u}_s, \tag{A.4}$$

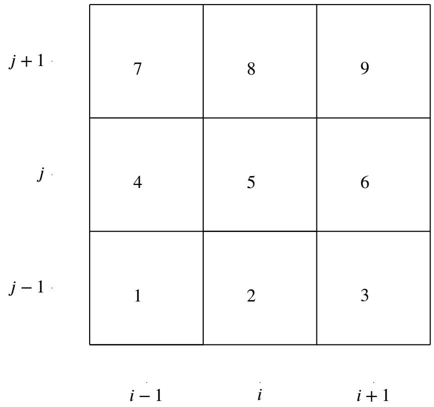

Fig. A.14. Stencil for the 3rd-order WENO-ZQ reconstruction.

where

$$
\begin{aligned}
&s=1,2 \quad \text{for} \quad k=1; \; s=2,3 \quad \text{for} \quad k=2;\\
&s=3,6 \quad \text{for} \quad k=3; \; s=6,9 \quad \text{for} \quad k=4;\\
&s=8,9 \quad \text{for} \quad k=5; \; s=7,8 \quad \text{for} \quad k=6;\\
&s=4,7 \quad \text{for} \quad k=7; \; s=1,4 \quad \text{for} \quad k=8.
\end{aligned}
$$

Step 3 Rewrite $q_0(x,y)$ as in [29,30,46,4]:

$$
q_0(x,y) = \gamma_0 \left(\frac{1}{\gamma_0} q_0(x,y) - \sum_{k=1}^{8} \frac{\gamma_k}{\gamma_0} q_k(x,y) \right) + \sum_{k=1}^{8} \gamma_k q_k(x,y), \tag{A.5}
$$

where $\{\gamma_k\}_{k=0}^{8}$ is a set of positive linear weights with their sum being 1. The linear weights control the balance between optimal reconstruction accuracy and avoiding numerical oscillation. In our numerical tests, we set $\gamma_0 = 0.6$ and $\gamma_1 = \ldots = \gamma_8 = 0.05$ for such balance.

Step 4 Compute the smoothness indicators of $\{q_k(x,y)\}_{k=0}^{8}$ [26]:

$$
\begin{aligned}
\beta_0 &= \frac{1}{\Delta x \Delta y} \sum_{l_1+l_2\le 2} \iint_{I_5} \left(\Delta x^{l_1} \Delta y^{l_2} \frac{\partial^{|l_1+l_2|}}{\partial_{l_1} \partial_{l_2}} q_0(x,y) \right)^2 dxdy,\\
\beta_k &= \frac{1}{\Delta x \Delta y} \sum_{l_1+l_2\le 1} \iint_{I_5} \left(\Delta x^{l_1} \Delta y^{l_2} \frac{\partial^{|l_1+l_2|}}{\partial_{l_1} \partial_{l_2}} q_k(x,y) \right)^2 dxdy, \text{for} \quad k=1,\ldots,8.
\end{aligned}
$$

The explicit expressions of $\{\beta_k\}_{k=0}^{8}$ are given by

$$
\begin{aligned}
\beta_0 &= \left(a_2^{q_0}\right)^2 + \left(a_3^{q_0}\right)^2 + \frac{13}{3}\left(a_4^{q_0}\right)^2 + \frac{7}{6}\left(a_5^{q_0}\right)^2 + \frac{13}{3}\left(a_6^{q_0}\right)^2,\\
\beta_k &= \left(a_2^{q_k}\right)^2 + \left(a_3^{q_k}\right)^2 \quad \text{for} \quad k=1,2,\ldots,8.
\end{aligned} \tag{A.6}
$$

Step 5 Compute the nonlinear weights $\{\omega_k\}_{k=0}^{8}$ [8,46]:

$$
\omega_k = \frac{\widetilde{\omega}_k}{\sum_{l=0}^{8} \widetilde{\omega}_l}, \tag{A.7}
$$

where

$$
\widetilde{\omega}_k = \gamma_k \left(1 + \frac{\tau^{\frac{3}{2}}}{\beta_k + \epsilon} \right) \quad \text{for} \quad k=0,1,\ldots,8 \tag{A.8}
$$

with

$$\tau = \frac{\sum_{k=1}^{8} |\beta_0 - \beta_k|}{8}. \tag{A.9}$$

When the exact solution is smooth over the entire large stencil $\bigcup_{s=1}^{9} I_s$ and $\Delta x \sim \Delta y$, we can prove

$$\omega_k = \begin{cases} \gamma_k \left(1 + O\left(\Delta x^{\frac{5}{2}}\right)\right), & \text{if } Du|_{(x_i,y_j)} \neq 0 \text{ and } D^2u|_{(x_i,y_j)} \neq 0, \\ \gamma_k \left(1 + O\left(\Delta x^2\right)\right), & \text{if } Du|_{(x_i,y_j)} = 0 \text{ and } D^2u|_{(x_i,y_j)} \neq 0, \end{cases}$$

by Taylor expansion.

Step 6 Construct the final reconstruction polynomial as follows:

$$u_{i,j}^{\text{WENO}}(x,y) = \omega_0 \left(\frac{1}{\gamma_0} q_0(x,y) - \sum_{k=1}^{8} \frac{\gamma_k}{\gamma_0} q_k(x,y) \right) + \sum_{k=1}^{8} \omega_k q_k(x,y). \tag{A.10}$$

Eventually, we define that $u^{\text{WENO}}(x,y)$ is the piecewise polynomial satisfying:

$$u^{\text{WENO}}(x,y) = u_{i,j}^{\text{WENO}}(x,y) \quad (x,y) \in I_{i,j} \quad \text{for all } i,j. \tag{A.11}$$

Remark A.1. $u^{\text{WENO}}(x,y)$ offers a 3rd-order approximation to $u(x,y,t)$, provided $\{\overline{u}_{i,j}\}$ is sufficiently accurate. Assuming $u(x,y,t)$ is sufficiently smooth and $\Delta x \sim \Delta y$, we can prove this as follows:

$$\begin{aligned}
& u_{i,j}^{\text{WENO}}(x,y) - u(x,y,t) \\
&= \left(\gamma_0 + \omega_0 - \gamma_0\right) \left(\frac{1}{\gamma_0} q_0(x,y) - \sum_{k=1}^{8} \frac{\gamma_k}{\gamma_0} q_k(x,y) \right) + \sum_{k=1}^{8} \left(\gamma_k + \omega_k - \gamma_k\right) q_k(x,y) \\
&\quad - \left(\sum_{k=0}^{8} \gamma_k + \sum_{k=0}^{8} \left(\omega_k - \gamma_k\right) \right) u(x,y,t) \\
&= \left(\omega_0 - \gamma_0\right) \left(\frac{1}{\gamma_0} \left(q_0(x,y) - u(x,y,t)\right) - \sum_{k=1}^{8} \frac{\gamma_k}{\gamma_0} \left(q_k(x,y) - u(x,y,t)\right) \right) \\
&\quad + q_0(x,y) - u(x,y,t) + \sum_{k=1}^{8} \left(\omega_k - \gamma_k\right) \left(q_k(x,y) - u(x,y,t)\right) \\
&= O(\Delta x^2) \left(O(\Delta x^3) + O(\Delta x^2)\right) + O(\Delta x^3) + O(\Delta x^2) O(\Delta x^2) \\
&= O(\Delta x^3), \qquad \text{for } (x,y) \in I_{i,j}.
\end{aligned}$$

Data availability

Data will be made available on request.

References

[1] T. Arbogast, C.-S. Huang, A fully conservative Eulerian–Lagrangian method for a convection–diffusion problem in a solenoidal field, J. Comput. Phys. 229 (9) (2010) 3415–3427.
[2] T. Arbogast, C.-S. Huang, C.-H. Hung, A fully conservative Eulerian-Lagrangian stream-tube method for advection-diffusion problems, SIAM J. Sci. Comput. 34 (4) (2012) B447–B478.
[3] U.M. Ascher, S.J. Ruuth, R.J. Spiteri, Implicit-explicit Runge-Kutta methods for time-dependent partial differential equations, Appl. Numer. Math. 25 (2) (1997) 151–167.
[4] D.S. Balsara, S. Garain, C.-W. Shu, An efficient class of WENO schemes with adaptive order, J. Comput. Phys. 326 (2016) 780–804.
[5] M. Benítez, A. Bermúdez, Numerical analysis of a second order pure Lagrange–Galerkin method for convection-diffusion problems. Part I: Time discretization, SIAM J. Numer. Anal. 50 (2) (2012) 858–882.
[6] M. Benitez, A. Bermudez, Numerical analysis of a second order pure Lagrange–Galerkin method for convection-diffusion problems. Part II: Fully discretized scheme and numerical results, SIAM J. Numer. Anal. 50 (6) (2012) 2824–2844.
[7] M. Benitez, A. Bermudez, Pure Lagrangian and semi-Lagrangian finite element methods for the numerical solution of convection-diffusion problems, Int. J. Numer. Anal. Model. 11 (2) (2014).
[8] R. Borges, M. Carmona, B. Costa, W.S. Don, An improved weighted essentially non-oscillatory scheme for hyperbolic conservation laws, J. Comput. Phys. 227 (6) (2008) 3191–3211.
[9] E. Boulais, T. Gervais, Two-dimensional convection-diffusion in multipolar flows with applications in microfluidics and groundwater flow, Phys. Fluids 32 (12) (2020) 122001.

[10] L. Braescu, T.F. George, Arbitrary Lagrangian-Eulerian method for coupled Navier-Stokes and convection-diffusion equations with moving boundaries, Appl. Math. Sci. Eng. (2007) 31–36.
[11] X. Cai, W. Guo, J.-M. Qiu, A high order semi-Lagrangian discontinuous Galerkin method for Vlasov–Poisson simulations without operator splitting, J. Comput. Phys. 354 (2018) 529–551.
[12] X. Cai, J.-M. Qiu, Y. Yang, An Eulerian-Lagrangian discontinuous Galerkin method for transport problems and its application to nonlinear dynamics, J. Comput. Phys. 439 (2021) 110392.
[13] Z. Chai, B. Shi, C. Zhan, Multiple-distribution-function lattice Boltzmann method for convection-diffusion-system-based incompressible Navier-Stokes equations, Phys. Rev. E 106 (5) (2022) 055305.
[14] J. Chen, J. Nakao, J.-M. Qiu, Y. Yang, A high-order Eulerian–Lagrangian Runge–Kutta finite volume (el–rk–fv) method for scalar nonlinear conservation laws, J. Sci. Comput. 102 (1) (2025) 12.
[15] J. Cheng, C.-W. Shu, A high order ENO conservative Lagrangian type scheme for the compressible Euler equations, J. Comput. Phys. 227 (2) (2007) 1567–1596.
[16] J. Cheng, C.-W. Shu, A high order accurate conservative remapping method on staggered meshes, Appl. Numer. Math. 58 (7) (2008) 1042–1060.
[17] B. Cockburn, C.-W. Shu, The local discontinuous Galerkin method for time-dependent convection-diffusion systems, SIAM J. Numer. Anal. 35 (6) (1998) 2440–2463.
[18] I. Cravero, M. Semplice, G. Visconti, Optimal definition of the nonlinear weights in multidimensional central WENOZ reconstructions, SIAM J. Numer. Anal. 57 (5) (2019) 2328–2358.
[19] N. Crouseilles, M. Mehrenberger, E. Sonnendrücker, Conservative semi-Lagrangian schemes for Vlasov equations, J. Comput. Phys. 229 (6) (2010) 1927–1953.
[20] M. Ding, X. Cai, W. Guo, J.-M. Qiu, A semi-Lagrangian discontinuous Galerkin (DG) – local DG method for solving convection-diffusion equations, J. Comput. Phys. 409 (2020) 109295.
[21] M. Dumbser, M. Käser, Arbitrary high order non-oscillatory finite volume schemes on unstructured meshes for linear hyperbolic systems, J. Comput. Phys. 221 (2) (2007) 693–723.
[22] A. Hidalgo, M. Dumbser, Ader schemes for nonlinear systems of stiff advection–diffusion–reaction equations, J. Sci. Comput. 48 (2011) 173–189.
[23] C.-S. Huang, T. Arbogast, An Eulerian–Lagrangian weighted essentially nonoscillatory scheme for nonlinear conservation laws, Numer. Methods Partial Differ. Equ. 33 (3) (2017) 651–680.
[24] C.-S. Huang, T. Arbogast, An implicit Eulerian–Lagrangian WENO3 scheme for nonlinear conservation laws, J. Sci. Comput. 77 (2) (2018) 1084–1114.
[25] G. Jacobs, W. Don, T. Dittmann, High-order resolution Eulerian–Lagrangian simulations of particle dispersion in the accelerated flow behind a moving shock, Theor. Comput. Fluid Dyn. 26 (2012) 37–50.
[26] G.-S. Jiang, C.-W. Shu, Efficient implementation of weighted ENO schemes, J. Comput. Phys. 126 (1) (1996) 202–228.
[27] P.H. Lauritzen, R.D. Nair, P.A. Ullrich, A conservative semi-Lagrangian multi-tracer transport scheme (CSLAM) on the cubed-sphere grid, J. Comput. Phys. 229 (5) (2010) 1401–1424.
[28] Y. Lee, B. Engquist, Multiscale numerical methods for passive advection–diffusion in incompressible turbulent flow fields, J. Comput. Phys. 317 (2016) 33–46.
[29] D. Levy, G. Puppo, G. Russo, Central WENO schemes for hyperbolic systems of conservation laws, Modél. Math. Anal. Numér. 33 (3) (1999) 547–571.
[30] D. Levy, G. Puppo, G. Russo, Compact central WENO schemes for multidimensional conservation laws, SIAM J. Sci. Comput. 22 (2) (2000) 656–672.
[31] J. Mackenzie, W. Mekwi, An unconditionally stable second-order accurate ALE–FEM scheme for two-dimensional convection–diffusion problems, IMA J. Numer. Anal. 32 (3) (2012) 888–905.
[32] J. Nakao, J. Chen, J.-M. Qiu, An Eulerian-Lagrangian Runge-Kutta finite volume (EL-RK-FV) method for solving convection and convection-diffusion equations, J. Comput. Phys. 470 (2022) 111589.
[33] M.M. Shoucri, A two-level implicit scheme for the numerical solution of the linearized vorticity equation, Int. J. Numer. Methods Eng. 17 (10) (1981) 1525–1538.
[34] C.-W. Shu, Essentially non-oscillatory and weighted essentially non-oscillatory schemes for hyperbolic conservation laws, in: Advanced Numerical Approximation of Nonlinear Hyperbolic Equations, Springer, 1998, pp. 325–432.
[35] R.N. Singh, Advection diffusion equation models in near-surface geophysical and environmental sciences, J. Indian Geophys. Union 17 (2013) 117–127.
[36] P.K. Smolarkiewicz, L.G. Margolin, MPDATA: a finite-difference solver for geophysical flows, J. Comput. Phys. 140 (2) (1998) 459–480.
[37] E.N. Sorensen, G.W. Burgreen, W.R. Wagner, J.F. Antaki, Computational simulation of platelet deposition and activation: I. Model development and properties, Ann. Biomed. Eng. 27 (4) (1999) 436–448.
[38] M. Spiegelman, R.F. Katz, A semi-Lagrangian Crank-Nicolson algorithm for the numerical solution of advection-diffusion problems, Geochem. Geophys. Geosyst. 7 (4) (2006).
[39] H. Wang, H.K. Dahle, R.E. Ewing, M.S. Espedal, R.C. Sharpley, S. Man, An ELLAM scheme for advection-diffusion equations in two dimensions, SIAM J. Sci. Comput. 20 (6) (1999) 2160–2194.
[40] Z. Wang, Y. Wang, Impact of convection-diffusion and flow-path interactions on the dynamic evolution of microstructure: arc erosion behavior of ag-sno2 contact materials, J. Alloys Compd. 774 (2019) 1046–1058.
[41] T. Xiong, J.-M. Qiu, Z. Xu, High order maximum-principle-preserving discontinuous Galerkin method for convection-diffusion equations, SIAM J. Sci. Comput. 37 (2) (2015) A583–A608.
[42] D. Xiu, G.E. Karniadakis, A semi-Lagrangian high-order method for Navier–Stokes equations, J. Comput. Phys. 172 (2) (2001) 658–684.
[43] X. Yang, B. Shi, Z. Chai, Generalized modification in the lattice Bhatnagar-Gross-Krook model for incompressible Navier-Stokes equations and convection-diffusion equations, Phys. Rev. E 90 (1) (2014) 013309.
[44] N. Zheng, X. Cai, J.-M. Qiu, J. Qiu, A fourth-order conservative semi-Lagrangian finite volume WENO scheme without operator splitting for kinetic and fluid simulations, Comput. Methods Appl. Mech. Eng. 395 (2022) 114973.
[45] L. Zhou, Y. Xia, Arbitrary Lagrangian–Eulerian local discontinuous Galerkin method for linear convection–diffusion equations, J. Sci. Comput. 90 (1) (2022) 21.
[46] J. Zhu, J. Qiu, A new fifth order finite difference WENO scheme for solving hyperbolic conservation laws, J. Comput. Phys. 318 (2016) 110–121.